



Provided by the author(s) and University of Galway in accordance with publisher policies. Please cite the published version when available.

Title	An updated experimental and kinetic modeling study of n-heptane oxidation
Author(s)	Zhang, Kuiwen; Banyon, Colin; Bugler, John; Curran, Henry J.; Rodriguez, Anne; Herbinet, Olivier; Battin-Leclerc, Frédérique; B'Chir, Christine; Heufer, Karl Alexander
Publication Date	2016-07-25
Publication Information	Zhang, Kuiwen, Banyon, Colin, Bugler, John, Curran, Henry J, Rodriguez, Anne, Herbinet, Olivier, Battin-Leclerc, Frédérique, B'Chir, Christine, Heufer, Karl Alexander (2016) 'An updated experimental and kinetic modeling study of n-heptane oxidation'. Combustion And Flame, 172 :116-135. doi: http://dx.doi.org/10.1016/j.combustflame.2016.06.028
Publisher	Elsevier ScienceDirect
Link to publisher's version	http://dx.doi.org/10.1016/j.combustflame.2016.06.028
Item record	http://hdl.handle.net/10379/6098
DOI	http://dx.doi.org/10.1016/j.combustflame.2016.06.028

Downloaded 2024-04-19T21:23:13Z

Some rights reserved. For more information, please see the item record link above.



An updated experimental and kinetic modeling study of *n*-heptane oxidation

Kuiwen Zhang¹, Colin Banyon¹, John Bugler¹, Henry J. Curran^{1*}
Anne Rodriguez,² Olivier Herbinet,² Frédérique Battin-Leclerc²
Christine B'Chir³, Karl Alexander Heufer³

¹*School of Chemistry, National University of Ireland Galway, Ireland*

²*Laboratoire Réactions et Génie des Procédés, CNRS, Université de Lorraine, ENSIC,
1, rue Grandville, BP 20451, 54001 Nancy Cedex, France*

³*Physico-Chemical Fundamentals of Combustion (PCFC), RWTH Aachen University, Schinkelstr. 8,
52062 Aachen*

Abstract

This work presents an updated experimental and kinetic modeling study of *n*-heptane oxidation. In the experiments, ignition delay times of stoichiometric *n*-heptane/air mixtures have been measured in two different high-pressure shock tubes in the temperature range of 726–1412K and at elevated pressures (15, 20 and 38 bar). Meanwhile, concentration versus time profiles of species have been measured in a jet-stirred reactor at atmospheric pressure, in the temperature range of 500–1100 K at $\varphi = 0.25, 2.0$ and 4.0 . These experimental results are consistent with those from the literature at similar conditions and extend the current data base describing *n*-heptane oxidation.

Based on our experimental observations and previous modeling work, a detailed kinetic model has been developed to describe *n*-heptane oxidation. This kinetic model has adopted reaction rate rules consistent with those recently developed for the pentane isomers and for *n*-hexane. The model has been validated against data sets from both the current work and the literature using ignition delay times, speciation profiles measured in a jet-stirred reactor and laminar flame speeds over a wide range of conditions. Good agreement is observed between the model predictions and the experimental data. The model has also been compared with several recently published kinetic models of *n*-heptane and shows an overall better performance. This model may contribute to the development of kinetic mechanisms of other fuels, as *n*-heptane is a widely used primary reference fuel. Since the sub-mechanisms of *n*-pentane, *n*-hexane and *n*-heptane have adopted consistent reaction rate rules, the model is more likely to accurately simulate the oxidation of mixtures of these fuels. In addition, the successful implementation of these rate rules have indicated the possibility of their application for the development of mechanisms for larger hydrocarbon fuels, which are of great significance for practical combustion devices.

Keywords: *n*-heptane, kinetic model, oxidation, shock tube, jet-stirred reactor

* Corresponding author Fax : +353 091 525700. E-mail: henry.curran@nuigalway.ie

1 Introduction

2 The oxidation of *n*-heptane has been widely studied as it is a primary reference fuel (PRF) and is
3 a representative normal alkane. It is also an important component of toluene reference fuel (TRF) and
4 ethanol toluene reference fuel (ERF) [1], which has been used as a surrogate gasoline fuel for research
5 of combustion processes in internal combustion engines [2]. Experiments have been performed which
6 have focused on different properties of fuel oxidation over a wide range of conditions, such as ignition
7 delay times in shock tubes [3-8] and rapid compression machines [9-12], species versus time and/or
8 temperature profiles measured in jet-stirred reactors [13-17] and flow reactors [18-21], laminar flame
9 speeds [22-26] and spatial distribution of species in flames [27-30]. Moreover, a series of experiments
10 have been performed in engines [31-35] to study homogeneous charge compression ignition (HCCI),
11 engine knock, exhaust gas recirculation (EGR), NO_x emission control, etc. Since 1979 [4] efforts have
12 been made to develop a kinetic model for *n*-heptane oxidation at both low temperature and high
13 temperature to provide further insight into this process. In 1989, Westbrook *et al.* developed a detailed
14 chemical kinetic mechanism to describe the oxidation of *n*-heptane and iso-octane [36]. This
15 mechanism adopted both low- and high-temperature chemistry, and was validated through comparisons
16 with experimental data from shock tube, turbulent flow reactor and jet-stirred reactors. Later, Chevalier
17 developed a computational technique to automatically develop detailed kinetic mechanisms, which
18 were used to study the influence of fuel, fuel mixtures and fuel additives on knock tendency [37]. Ranzi
19 *et al.* proposed a semi-detailed kinetic model for *n*-heptane oxidation [38], while Côme used a computer
20 package to develop the kinetic models for the oxidation of both *n*-heptane and iso-octane [39].

21 Curran *et al.* [40] carried out a comprehensive kinetic modeling study of *n*-heptane oxidation in a
22 systematic way. The important reactions during the oxidation of *n*-heptane were categorized into 25
23 different reaction classes, including 10 reaction classes to describe high-temperature oxidation and 15
24 classes to describe the low-temperature regime. Although approximate treatments were assigned to
25 some less important reactions such as the consumption of the heptene isomers, the overall performance
26 of the mechanism was very good. This mechanism has been improved and further validated, with good
27 performance over the pressure range of 3 to 50 atm, in the temperature range of 650 to 1200 K and at
28 equivalence ratios of 0.3 to 2.0. More importantly, this model set a successful frame for the kinetic
29 mechanism development of other larger *n*-alkanes [41]. A more recent study carried out by Mehl *et al.*
30 [42] on the kinetic modeling of gasoline surrogate components and mixtures under engine conditions
31 has further refined and adopted this mechanism. Moreover, this mechanism also forms the basis for the
32 mechanism development in this work.

33 There has been a continual interest among the research community in developing a better
34 understanding of *n*-heptane oxidation both experimentally and theoretically. For example, Herbinet *et al.*
35 performed an experimental study in a jet-stirred reactor [16]. In addition to traditional gas
36 chromatography, the experiments also used synchrotron vacuum ultraviolet photoionization mass
37 spectrometry as the diagnostic technique to identify the unstable species such as radicals, which is an

1 example of the new experimental methods being applied to this kind of study. Herbinet *et al.* also
2 generated a kinetic mechanism using the software EXGAS [43], which satisfactorily reproduced the
3 mole fraction profiles of most of the species identified in the experiments.

4 Meanwhile, new reaction pathways are being adopted into the kinetic model to better describe the
5 oxidation process of *n*-heptane. Recently, Pelucchi *et al.* proposed an improved kinetic model for *n*-
6 heptane [44], by emphasizing new reaction classes producing organic acids, diones and ketones in the
7 low temperature regime. The mechanism was validated over a wide range of conditions including both
8 low and high-temperature ranges. Good agreement was observed between simulations and experimental
9 data from the literature for ignition delay time measurements [5, 42, 45], species profiles measurements
10 taken in a jet-stirred reactor [14-16] and in a flow reactor [20], as well as laminar flame speeds [26].
11 Meanwhile, the experimental database of *n*-heptane is being extended to cover a wider range of
12 conditions. Seidel *et al.* performed an experimental and kinetic modeling study of a fuel-rich, premixed
13 *n*-heptane flame at 40 mbar, and successfully identified over 80 species generated at this condition [30].
14 Based on previous work, a detailed kinetic model was developed. Reduced kinetic mechanisms are also
15 being proposed, such as the work by Cai and Pitsch [46], who proposed an optimized chemical
16 mechanism for gasoline surrogates which was validated under extensive conditions and it showed a
17 very good performance compared to experimental ignition delay measurements.

18 This current study is based on a continuity of effort in experimental and kinetic modeling studies
19 of hydrocarbon fuels that we have published previously [47-58]. In this work, the ignition delay times
20 of *n*-heptane in air are firstly measured in two different high-pressure shock tubes to provide more
21 experimental ignition delay time data at elevated pressures. Moreover, the experimental conditions of *n*-
22 heptane oxidation in a jet-stirred reactor have been extended to extremely rich ($\phi = 4.0$) and very lean
23 ($\phi = 0.25$) conditions, while the other conditions remain consistent with those published previously. To
24 reflect the improvements in the chemical kinetics and thermodynamics as well as their impact, a
25 detailed kinetic model of *n*-heptane oxidation has been developed based on our previous work,
26 including our updated base mechanism [47-50, 53, 56-58], the sub-mechanisms of the pentane isomers
27 [51, 55] and *n*-hexane [54]. In the development of this mechanism, the new reaction classes and
28 reaction rate rules with modifications, which have been successfully applied to the pentane isomers and
29 *n*-hexane, have been adopted. The thermodynamic database has also been updated with recently
30 published optimized group values [52]. The model has been validated using the experimental data sets
31 obtained in this work, as well as those from the literature for ignition delay times, species profile
32 measured in jet-stirred reactors and also for laminar flame speed measurements. Moreover, comparisons
33 are made between the current model and those from recent publications. The significant reaction
34 pathways for the oxidation of *n*-heptane are revealed by further analysis of the simulations.

35

1 **Experimental Methods**

2 *PCFC Shock tube*

3 The Physico-Chemical Fundamentals of Combustion (PCFC) shock tube at Aachen University has been
4 designed similar to the high-pressure shock tube at NUIG. It has an inner diameter of 63.5 mm and an
5 overall length of about 7.5 m with a 3 m driver section. Due to physical space limitations the driver
6 section is curved with a bending radius of 1 m. The diaphragm section can house up to two pre-scored
7 aluminum diaphragms. All parts coming into contact with fuel/air mixtures are made of stainless steel
8 (316Ti), except for the aluminum diaphragms. Shock velocities and pressure profiles are recorded in the
9 measuring section close to the endwall of the driven section with up to 8 PCB 113B22 pressure sensors.
10 Signals are recorded using a digital oscilloscope with a sampling rate of 25 MHz. Fuel/air mixtures are
11 prepared in a separate 40 L Teflon coated stainless steel mixing vessel. Partial pressures are used to
12 prepare the desired gas mixtures. Static pressures are monitored with two STS ATM. 1st pressure
13 sensors with measuring ranges of 500 mbar and 5 bar, respectively. The shock tube, manifold and
14 mixing vessel can be electrically heated to 150 °C in order to avoid fuel condensation. In this study,
15 initial temperatures of 40 °C are sufficient due to the relatively high vapor pressure of *n*-heptane.
16 Temperatures are monitored with type T thermocouples due to their lower measuring uncertainty
17 compared to conventional type K ones. High purity grade gases for reactive mixture preparation (N₂ and
18 O₂) were provided from Praxair and Westfalia. Helium and compressed air were used as driver gases.
19 The reflected shock conditions were calculated using the initial conditions of pressure and temperature
20 and mixture composition and the measured shock velocity with an in-house code which is based on the
21 shock and detonation toolbox [59] in Cantera [60]. An uncertainty analysis has been performed for the
22 PCFC shock tube and is provided as Supplementary material. Maximum uncertainties in the reflected
23 shock temperatures are estimated to amount to 1.1% in the reflected shock temperature and 3.5% in the
24 reflected shock pressure. Depending on the fuel reactivity this can induce uncertainties of up to 15% in
25 the measured ignition delay time for the range studied.

26 *NUIG Shock tube*

27 High-temperature (above 1000 K) ignition delay times for stoichiometric mixtures of *n*-heptane
28 at compressed pressures of 15 bar in a 21% O₂ : 79% N₂ bath gas were measured in the National
29 University of Ireland, Galway (NUIG) high-pressure shock tube [61], with an inner diameter of 63 mm.
30 The methodology used to measure ignition delay times in this facility has recently been described in our
31 work on *n*-hexane [54], and thus will not be described further here. Again, *n*-heptane was supplied by
32 TCI UK in high purity (> 99.0%), while oxygen (99.5%) and nitrogen (99.95%) were supplied by BOC
33 Ireland.

34

1 *Jet-stirred reactor*

2 The oxidation of *n*-heptane was studied in a jet-stirred reactor at LRGP in Nancy (France). This
3 reactor can be considered to be perfectly stirred [62] and has frequently been used for numerous gas
4 phase kinetic oxidation studies of hydrocarbons and oxygenated compounds [63]. Experiments were
5 performed at a constant pressure of 1.067 bar, at a residence time of 2 s, at temperatures ranging from
6 500 to 1100 K, and at four equivalent ratios of $\varphi = 0.25, 1.0, 2.0$ and 4.0. The fuel was diluted in helium
7 resulting in an *n*-heptane concentration of 0.5%. The fuel was provided by Sigma-Aldrich (purity of
8 99%). Helium and oxygen were provided by Messer with purities of 99.99% and 99.999%, respectively.

9 The reactor is made of fused silica, and consists of a fused silica sphere (volume = 95 cm³) into
10 which diluted reactant enters through an injection cross located at its center. It is operated at constant
11 temperature and pressure and it is preceded by an annular pre-heating zone in which the temperature of
12 the gases is increased to the reactor temperature before entering it. The gas mixture residence time
13 inside the annular pre-heater is very short compared to its residence time inside the reactor (a few
14 percent). Both the spherical reactor and the annular pre-heating zone are heated using resistance wires
15 coiled around their walls. The temperature is controlled using type K thermocouples. The reaction
16 temperature was measured using another independent type K thermocouple which was located in a
17 glass finger at the center of the reactor (which is actually the intra annular part of the preheater). The
18 uncertainty in the temperature measurement is ± 5 K.

19 A Coriolis flow controller is used to feed *n*-heptane, and two mass flow controllers are used to
20 meter the helium and oxygen flow rates. The fuel is mixed with helium and evaporated in a heat
21 exchanger. Oxygen is added at the reactor inlet. The accuracy in flow rates given by the manufacturer
22 (Bronkhorst) is 0.5%. This results in a small uncertainty of 2.00 ± 0.01 s in the residence time.

23 Product species are analyzed directly by gas chromatography using a heated transfer line between
24 the reactor outlet and the chromatograph sampling. The temperature of the line is heated to 160 °C to
25 avoid product condensation during transfer. Three gas chromatographs are used for the quantification of
26 the different species. The first chromatograph, equipped with a Carbosphere packed column, a thermal
27 conductivity detector (TCD) and a flame ionization detector (FID), is used for the quantification of O₂,
28 CO, CO₂, methane, ethylene, acetylene and ethane. The second is fitted with a PlotQ capillary column,
29 a methanizer, and an FID is used for the quantification of molecules from methane to reaction products
30 containing up to 5 carbon atoms and 1 or 2 oxygen atoms maximum. The third is fitted with a HP-5
31 capillary column and an FID is used for the quantification of molecules which contain at least 5 carbon
32 atoms. Calibrations are performed by injecting standards where available or by using the effective
33 carbon number method when standards were unavailable. The maximum relative error in mole fractions
34 is estimated to be $\pm 5\%$ for species which are calibrated using standards and $\pm 10\%$ for species calibrated
35 using the effective carbon number method [64-65]. The identification of reaction products is performed
36 using a gas chromatograph equipped with a PlotQ or an HP-5 capillary column and coupled to a mass
37 spectrometer (quadrupole). The mass spectra of all of the detected reaction products are included in the

1 NIST 08 Mass Spectra Database [66]. For certain species, single-photon-ionization mass spectrometry
2 (SPI-MS) [67] is used for higher accuracy, as shown in the experimental data sets provided in the
3 Supplementary material.

4 **Chemical Kinetic Mechanism**

5 The kinetic model used in this work consists of 1268 species and 5336 reactions. The sub-
6 mechanism for C₀–C₄ fuels is taken from AramcoMech 2.0 [57-58]. This mechanism has been widely
7 validated for a series of fuels including hydrogen, syngas [48], methane, methanol [56], formaldehyde,
8 ethane, ethylene, acetylene, ethanol, acetaldehyde [47], dimethyl ether [53] and propene [49-50]. The
9 sub-mechanisms for the three pentane isomers and for *n*-hexane have also been published recently [51,
10 54-55]. On the basis of the above mechanisms, an *n*-heptane sub-mechanism has been developed in this
11 work. Table 1 shows the nomination of some representative species in the *n*-heptane sub mechanism.

12 Figure 1 shows the reaction pathways for *n*-heptane oxidation considered in this work, which are
13 similar to those considered previously [40, 51, 54]. The reaction pathways of a fuel are strongly
14 dependent on its structure, and significantly affect the reactivity of the fuel. Compared to smaller
15 alkanes, *n*-pentane shows a higher reactivity at low temperatures because its structure contains more
16 connected secondary carbons. H-atom abstraction is favored at secondary sites compared to primary
17 ones, where secondary pentyl peroxy radicals formed can isomerize via six-membered transition state
18 (TS) rings into hydroperoxy pentyl radicals. Six-membered TS ring formations are faster than any other
19 (5-, 7-, or 8-membered ones) which is mainly due to their lower ring-strain energy and formation of six-
20 membered TS ring structures contributes considerably to the chain branching process at low
21 temperatures, promoting fuel reactivity [51, 54-55]. Similarly, *n*-hexane shows a higher reactivity
22 compared to *n*-pentane because six-membered TS ring structures are available for all of the four
23 connected secondary carbons, while the reactivity of *n*-heptane is even higher than that of *n*-hexane
24 since the ratio of secondary carbon atoms to primary ones is even higher again. However, the reaction
25 pathways that need to be considered for *n*-pentane, *n*-hexane and *n*-heptane are almost identical, as
26 shown in Fig. 1. Therefore consistent reaction rate rules can be applied to their sub-mechanisms.

27 A series of reaction rate rules have been adopted in our previous work on the oxidation of the
28 pentane isomers [51, 55]. These rate rules were derived from recently published ab-initio calculations
29 [68-73] and have been applied to the reaction classes in the low temperature regime. New reaction
30 classes related to the alternative isomerization pathway of peroxy hydroperoxyl alkyl radicals [51] have
31 also been added. The mechanisms for the three pentane isomers predict well ignition delay times with
32 good agreement observed compared to the experimental data [55]. Many of the rate constants for the
33 low temperature reaction classes (e.g. $\text{RO}_2 \rightleftharpoons \dot{\text{Q}}\text{OOH}$, etc.) for the pentane isomers are available from
34 ab-initio calculations [68, 71-72], but those for the hexane isomers and larger alkanes are rare.
35 Therefore in the kinetic modeling study of *n*-hexane, the reaction rate rules were derived from those
36 calculated for *n*-pentane but modifications were made within their uncertainty range, which have led to

1 better agreement between the experimental and simulated results [54]. The refined rate rules have been
2 used to generate the *n*-heptane mechanism used in this work to maintain consistency in the chemical
3 kinetics.

4 The thermodynamic data of the species involved have been updated using the THERM software
5 [74], which is based on the group additivity method proposed by Benson [75]. The group values used in
6 the calculation have been optimized [52], and are consistent with those used for the pentane isomers and
7 for *n*-hexane [51, 54-55]. The kinetic mechanism, thermodynamic data, transport data, species glossary
8 and group values for group additivity method are available as Supplementary material. In the future,
9 this mechanism might be updated for better performance and released with comprehensive validations.
10 Please visit our website <http://c3.nuigalway.ie/> for more details.

11 *High temperature mechanism*

12 The most significant reaction classes in the high temperature regime of *n*-heptane oxidation are
13 the unimolecular decomposition of the fuel and fuel derived radicals in addition to hydrogen abstraction
14 from the fuel by the radical pool. To derive the rate constants for the unimolecular decomposition of *n*-
15 heptane, firstly the high-pressure limit rate constants of the radical recombination are estimated; then
16 the reverse rate constants are obtained using the CHEMRev software package [76] with their pressure
17 dependence calculated using Quantum-Rice-Ramsperger-Kassel/Modified Strong Collision
18 (QRRK/MSK) theory, which has been proven to show good agreement with the more precise Rice-
19 Ramsperger-Kassel-Marcus/Master Equation (RRKM/ME) approach for alkane decomposition [77].
20 The Lennard-Jones parameters for *n*-heptane are from Jasper and Miller [78], which are $\sigma = 4.42 \text{ \AA}$ and
21 $\varepsilon = 213 \text{ cm}^{-1}$ in a bath gas of N_2 . The pressure dependent rate constants for the decomposition of the
22 fuel-derived radicals: $\dot{\text{C}}_7\text{H}_{15-1}$, $\dot{\text{C}}_7\text{H}_{15-2}$ and $\dot{\text{C}}_7\text{H}_{15-3}$ are adopted from [79].

23 H-atom abstraction from the fuel by $\dot{\text{O}}\text{H}$ radicals is the most significant reaction class involving
24 the fuel with the radical pool over a wide temperature range. The rate constants for these reactions have
25 been adopted from the values reported by Sivaramakrishnan and Michael [80], who measured these
26 reaction rates experimentally in a shock-tube using $\dot{\text{O}}\text{H}$ -radical electronic absorption and compared the
27 results with literature data. H-atom abstraction by $\dot{\text{H}}\text{O}_2$ radicals contributes little to fuel consumption at
28 low temperatures (600–750 K) but these reactions become more important at higher temperatures (750–
29 1300 K) because the H_2O_2 molecule produced decomposes into *two* $\dot{\text{O}}\text{H}$ radicals, greatly promoting
30 reactivity. The rate constants for H-atom abstraction from the fuel by $\dot{\text{H}}\text{O}_2$ radicals are adopted from
31 [81], other reactions in the high temperature regime and their rate constants are mainly derived from the
32 *n*-heptane mechanism proposed by Curran *et al.* [40].

33

1 *Low temperature mechanism*

2 The low-temperature reaction pathways are illustrated in the upper part of Fig. 1. In the low-
3 temperature regime, the fuel derived radicals (\dot{R}) add to molecular oxygen to form alkylperoxy radicals
4 ($R\dot{O}_2$). Further isomerization of $R\dot{O}_2$ via ring transition states and internal hydrogen atom transfer leads
5 to the formation of hydroperoxy-alkyl radicals ($\dot{Q}OOH$). The most important competing reaction class
6 is the concerted elimination forming C7 olefins and $H\dot{O}_2$ radicals, which becomes more competitive as
7 the temperature increases. At low- and intermediate-temperatures this concerted elimination reaction
8 tends to reduce reactivity, because it consumes a reactive radical (usually $\dot{O}H$) in the hydrogen
9 abstraction reaction from the fuel, and produces an $H\dot{O}_2$ radical which is less reactive. Other
10 consumption reactions of $R\dot{O}_2$ are bi-molecular reactions, but only play a minor role in the reaction flux.
11 For the consumption of $\dot{Q}OOH$ radicals, the addition to molecular oxygen is a significant step,
12 producing peroxy alkylhydroperoxide radicals (\dot{O}_2QOOH) as the precursor of ketohydroperoxides. $\dot{O}H$
13 radicals are produced from both the formation and decomposition of ketohydroperoxides, which make
14 this reaction sequence the major chain branching process at low temperatures. Meanwhile, the
15 consumption of $\dot{Q}OOH$ radicals also has other channels. As the O–O bond in the hydroperoxy group is
16 weak, the consumption of $\dot{Q}OOH$ radical can produce small molecule products or cyclic ethers and
17 release an $\dot{O}H$ radical, which contributes to the chain propagation process. The beta-scissions of C–O
18 bonds that produce olefins and HO_2 radicals are only available for certain structures such as
19 $C_7H_{14}OOH_{1-2}$ and are thus less important.

20 The equilibrium between $R\dot{O}_2$ and $\dot{Q}OOH$ radicals significantly influences fuel reactivity at low-
21 and intermediate-temperatures. The concerted elimination reaction of $R\dot{O}_2$ leads to chain propagation
22 while the addition of $\dot{Q}OOH$ radicals to O_2 ultimately contributes to chain branching. Other significant
23 reaction classes that can affect this equilibrium include the addition of \dot{R} to O_2 , the formation of cyclic
24 ethers and the formation of ketohydroperoxides. The modified reaction rate rules for the above
25 mentioned reaction classes are consistent with those proposed for *n*-hexane [54], as shown in Table 2.
26 Detailed discussions of the comparison of rate rules and the refinements can be found elsewhere [51].

27 The red open arrows in Fig. 1 denote the reaction classes induced by the alternative isomerization
28 pathways of \dot{O}_2QOOH radicals. These reaction classes have been proposed in our previous work [51,
29 54], with their reaction rate constants taken by analogy with those possible for $R\dot{O}_2$ radicals. Although
30 the adoption of alternative isomerization pathways has proven to have a limited effect upon model
31 predictions for *n*-hexane [54], these reaction classes have been included for *n*-heptane to reflect the
32 complexity of the low temperature chemistry, which become more important for the oxidation of
33 branched alkanes [51].

34

1 **Results and discussion**

2 *High pressure shock tube data*

3 The ignition delay times for the oxidation of stoichiometric *n*-heptane/air mixtures at different
4 pressures have been measured in the PCFC high pressure shock tube, see solid symbols in Fig. 2, over
5 the temperature range of 688–1412 K, which includes the low, intermediate and high temperature
6 regimes. The new data sets are consistent with those reported in previous work [82-83] which are
7 depicted as half-filled symbols and open symbols respectively, showing a significant pressure effect
8 reflected by the decrease in ignition delay times and the shifting of the negative temperature coefficient
9 (NTC) region towards higher temperatures [5] at higher pressures. Furthermore, simulation results
10 using the kinetic mechanism presented in this study are shown. Shock tube ignition delay times are
11 simulated using the constant volume closed homogenous batch reactor code in CHEMKIN PRO [84]. It
12 is assumed that the changes in conditions induced by facility effects in the region near the endwall can
13 be treated as an isentropic compression/expansion by an effective volume change as in the RCM. These
14 CHEMKIN PRO input files and the experimental data are available as Supplementary material. In the
15 following descriptions, the ignition event in the simulation is defined as the maximum pressure rise
16 unless the experimental data sets taken from literatures define the ignition delay differently.

17 It is important to note that the different data sets have been obtained in different facilities. This is
18 a critical aspect regarding the level of confidence of the experimental results. By considering results
19 taken at the same conditions but from different facilities, a higher level of confidence can be attributed
20 to the experimental results. This has motivated a repeat of experiments in this study at conditions that
21 have been reported previously.

22 Another aspect of this investigation is the treatment of facility effects. The conditions such as
23 pressure and temperature behind the reflected shock are ideally constant. However, in the real process
24 both the pressure and temperature behind the reflected shock increase with time due to boundary layer
25 effects inside the shock tube and the non-ideal opening of diaphragms. This leads to pressure and
26 temperature gradients influencing the ignition process. As a result, the measured ignition delay times
27 may be shorter than those assuming ideal conditions. More detailed discussion on these shock tube
28 facility effects can be found in [85]. In general, these effects become stronger with smaller inner
29 diameter tubes and longer measuring times. In Fig. 2 the results of shock tubes with inner diameters of
30 50 mm [83], 63.5 mm (this study) and 140 mm [82] are shown. In [82] an average pressure gradient of
31 $p/p_0 = 3\%/ms$ is given for the 140 mm tube. The PCFC tube has an average pressure gradient of $8\%/ms$
32 due to the smaller inner diameter. This pressure gradient has been determined from non-reactive
33 measurements (Fig. 3). Pressure gradients of the 50 mm tube have previously been reported to amount
34 to around $10\%/ms$ [85].

35 At high pressures, where ignition delay times are well below 1 ms, these different pressure
36 gradients hardly have an effect on ignition delay times and in this case the simulations can be performed
37 assuming a truly constant volume reactor. For longer measuring times above 1 ms, facility effects are

1 taken into account by assuming a volume change reflecting the experimentally observed constant
2 increase in pressure as appropriate, depending on the shock tube as discussed above. Comparing the
3 experimental results with the kinetic simulation including a proper treatment of the facility induced
4 increase in pressure and temperature, it becomes obvious that the mechanism is able to predict the
5 measured ignition delay times within 15%, which is within the experimental uncertainty.

6 It can be seen in Fig. 2 that the model predicts well the measured ignition delay times when the
7 facility effect is considered (solid lines). The previous and current results appear inconsistent in ignition
8 delay times at 38 bar, because both the current experiments and simulations were not performed at
9 precisely 38 bar as in [82] (see the experimental data in the Supplementary material). Therefore the
10 inconsistency is caused by the pressure effect. By using the specific experimental temperatures and
11 pressures in our simulations, the model can successfully reproduce both the current and the previous
12 experimental results. It is worth noting that the simulations using varying volume traces obtained from
13 the experimentally measured non-reactive pressure profiles are very similar to those assuming an
14 average constant increase in pressure of 8%/ms, which is consistent with the average pressure gradient
15 of 7–8%/ms assumed for the PCFC shock tube. The dashed lines in Fig. 2 represent the simulations
16 with the current mechanism using unmodified rate rules, which tend to under-predict ignition delay
17 times over the entire temperature range. This trend is similar to those observed in the kinetic and
18 modeling study of *n*-hexane [54].

19 As an additional input to the ignition delay times at higher temperature, Fig. 4 shows the ignition
20 delay times measured in the high-pressure shock tube at NUIG for *n*-heptane oxidation at $\phi = 1.0$ and
21 15 bar in the temperature range 1058–1298 K. The agreement between the experimental (points) and
22 modeling results (solid line) are good, which further validates the high temperature *n*-heptane chemistry.
23 The dashed line shows model simulations with unmodified rate rules. The slight difference between the
24 predictions indicates that those modifications have only a minor effect in this temperature regime.

25 The mechanism has also been validated using shock tube ignition delay time data from the
26 literature. Campbell et al [86] used a shock tube to measure ignition delay times for *n*-heptane oxidation
27 in the temperature range 651–823 K and at pressures between 6.1 and 7.4 atm at $\phi = 0.75$ in 15%
28 O₂/5%CO₂/Ar and in 15% O₂/Ar mixtures. Both first-stage (cool flame) and second-stage (total)
29 ignition delay times were measured, providing critically needed targets for further validation of kinetic
30 models. Figure 5 shows the experimental and modeling results for that study [86] which used the LLNL
31 mechanism [42], and the predictions using the current model as well as several other models [16, 30,
32 46]. It can be seen that the current mechanism generally shows a better performance in predicting both
33 the first and the second stage ignition delay times.

34 Shen et al. [45] measured ignition delay times for several *n*-alkane/air mixtures in a heated shock
35 tube. The experimental results for *n*-heptane, which were measured at $\phi = 0.25, 0.5$ and 1.0 at multiple
36 pressures are shown in Fig. 6. These results show the varying reactivity of *n*-heptane depending on
37 temperature, pressure and equivalence ratio, which have been well captured by the current model. Here

1 the maximum in excited OH radical concentration is defined as the ignition delay event, which is
 2 consistent with that reported in [45]. Some discrepancies can be seen at conditions such as $\varphi = 0.5$ at 13
 3 atm. However, the relevant experimental data is not completely consistent with those under similar
 4 conditions shown in Fig. 7. Therefore these discrepancies can be partly attributed to the uncertainties of
 5 some specific data points from the literature. Ciezki and Adomeit investigated the ignition delay times
 6 for *n*-heptane/air mixtures in a high pressure shock tube for equivalence ratios of 0.5 to 3.0, at pressures
 7 between 3.2 and 42 bar in the temperature range of 660–1350 K [5]. These experimental data have been
 8 the benchmark for validating *n*-heptane oxidation mechanisms [16-17, 30, 40, 42, 44] for many years.
 9 Figure 7 shows a comparison of the experimental results reported by Ciezki and Adomeit and the
 10 predictions using the current mechanism, which indicates that it captures well the trend of the reactivity
 11 with the varying equivalence ratio, pressure and temperature ranges. The comparison of the predictions
 12 using the current mechanism and several other recently published ones [16, 30, 42, 44, 46] are shown in
 13 Fig. 8 (a), (b), (c), (d) and (e) respectively.

14 A brute force sensitivity analysis was performed using CHEMKIN PRO [84] at $\varphi = 1.0$, $p = 20$
 15 bar, $T = 720$ K, and at 820 K and 1000 K respectively to determine the reactions that are most
 16 significant for the ignition process, Fig. 9. In the analysis, the rate constants of each reaction were
 17 increased and decreased by a factor of two (k_+ and k_-), and the simulations were performed using two
 18 mechanisms adopting these changes to obtain the ignition delay times (τ_+ and τ_-). The sensitivity
 19 coefficient (S) is then defined as follows:

$$20 \quad S = \frac{\ln(\tau_+/\tau_-)}{\ln(k_+/k_-)} = \frac{\ln(\tau_+/\tau_-)}{\ln(2/0.5)}$$

21 From the definition above, it can be concluded that a reaction with a positive sensitivity
 22 coefficient inhibits reactivity while that with a negative sensitivity coefficient promotes reactivity.

23 At low temperatures, the consumption of the fuel is mainly initiated by H-atom abstraction from
 24 the fuel by $\dot{\text{O}}\text{H}$ radicals, followed by propagation via addition to $\text{O}_2 \rightarrow$ isomerization to $\dot{\text{Q}}\text{OOH} \rightarrow$
 25 addition to O_2 , and the branching process via the formation and decomposition of ketohydroperoxides
 26 which produce $\dot{\text{O}}\text{H}$ radicals, promoting reactivity. Therefore at low temperatures, the reactivity is
 27 dominated by chain branching from the fuel, depicted in Fig. 9 (a). Hydrogen and other small species
 28 chemistry is only of minor importance. The most significant reactions promoting reactivity are those
 29 leading to the formation and decomposition of ketohydroperoxides. However, the formation of
 30 ketohydroperoxides via the isomerizations of $\dot{\text{O}}_2\text{QOOH}$ radicals is not sensitive, because at low
 31 temperatures this reaction class dominates the consumption of $\dot{\text{O}}_2\text{QOOH}$ radicals, while other
 32 consumption pathways such as the beta-scissions of $\dot{\text{Q}}\text{OOH}$ radicals cannot compete with their addition
 33 to molecular oxygen, even when their A factors are reduced by a factor of two. The newly adopted
 34 alternative isomerization reactions of $\dot{\text{O}}_2\text{QOOH}$ radicals only show minor contributions as discussed in
 35 a previous work [54].

1 *n*-Heptane composes only primary and secondary carbon atoms. H-atom abstraction from fuel by
2 the radical pool mainly occurs at secondary carbon sites because the C–H bonds are weaker compared
3 to those on primary carbons. For the same reason, the hydrogen atoms on secondary carbons are
4 favored for the internal H-atom transfer/abstraction process in the isomerization of $\dot{R}O_2$ to $\dot{Q}OOH$
5 radicals. Meanwhile, the isomerization of $\dot{R}O_2$ to $\dot{Q}OOH$ radicals prefers six-membered ring transition
6 states since they have the lowest ring strain energies. These preferences of relevant reaction classes are
7 also reflected in Fig 9 (a). For example, the most sensitive reaction promoting reactivity is the addition
8 of $\dot{C}_7H_{14}OOH_{2-4}$ radicals to O_2 . These are produced through the sequence of hydrogen abstraction from
9 a secondary carbon \rightarrow addition to $O_2 \rightarrow$ isomerization via a six-membered transition state ring and
10 internal abstraction of a secondary H-atom. The decomposition of the relevant ketohydroperoxide,
11 C7KET24, also significantly promotes reactivity. Similarly, the additions of $\dot{C}_7H_{14}OOH_{3-5}$ and
12 $\dot{C}_7H_{14}OOH_{4-2}$ radicals to O_2 also contribute significantly to reactivity, with certain differences caused
13 by the branching ratios of hydrogen abstraction reactions from the fuel. On the other hand, the
14 concerted (olefin + $\dot{H}O_2$ radical) elimination reactions are the most inhibiting at low temperatures.
15 Although $\dot{H}O_2$ radicals can abstract hydrogen atoms from the fuel, these reactions are considerably
16 endothermic and contribute little to fuel consumption at low temperatures. In addition, H-atom
17 abstraction from the fuel by $\dot{H}O_2$ radicals produces H_2O_2 which only decomposes easily into $\dot{O}H$
18 radicals at higher temperatures (~ 850 K). As has been discussed above, the equilibrium between $\dot{R}O_2$
19 and $\dot{Q}OOH$ radicals significantly influences fuel reactivity at low temperatures. This is consistent with
20 Fig. 9 (a) since the concerted elimination reactions of $\dot{R}O_2$ play a key role in reducing reactivity, while
21 the addition of $\dot{Q}OOH$ to O_2 greatly increases it. The predicted reactivity of *n*-heptane (Fig. 2) and *n*-
22 hexane [54] become lower when modified reaction rate rules are used, which can be mainly attributed
23 to the enhanced concerted elimination reactions in the modification [54].

24 Figure 9 (b) shows the results of the sensitivity analysis performed in the NTC region at 820 K.
25 With an increase in temperature, there is an increased competition between chain branching and chain
26 propagation/termination reactions. Under these conditions, the addition of $\dot{Q}OOH$ radicals to O_2 and the
27 concerted elimination reactions of $\dot{R}O_2$ radicals continue to be important promoting and inhibiting
28 reaction classes, respectively. However, the chemistry of small molecules starts to become important.
29 The most important reaction promoting reactivity is the decomposition of H_2O_2 , while the most
30 inhibiting reaction is the chain termination reaction $\dot{H}O_2 + \dot{H}O_2 = H_2O_2 + O_2$. This is because in this
31 reaction two $\dot{H}O_2$ radicals are consumed to produce just one H_2O_2 molecule leading to the formation of
32 *two* reactive $\dot{O}H$ radicals, whereas if one $\dot{H}O_2$ radical reacts with any stable species two radicals and
33 two H_2O_2 molecules will be produced leading to the formation of *four* reactive $\dot{O}H$ radicals. Moreover,
34 even though the decomposition of H_2O_2 into $\dot{O}H$ radicals promotes reactivity, this reaction is
35 endothermic and only becomes significant at higher temperatures. At 820 K, $\dot{H}O_2$ radicals can also be
36 converted into more reactive $\dot{O}H$ radicals via reaction with $\dot{C}H_3$ and $\dot{C}H_3O_2$ radicals, promoting
37 reactivity as shown in Fig. 9 (b), or inhibit reactivity through the chain-termination reaction producing

1 H₂O₂ and O₂. However, the temperature can increase to temperatures above 900 K after the first stage
2 ignition, making the decomposition of H₂O₂ much easier and promoting reactivity. The sensitivity
3 coefficients shown in Fig. 9 (b) reflect the influences of different reactions integrated over the entire
4 ignition process. It indicates that the production and consumption reactions of HO₂ radicals play a
5 significant role in the NTC region, and are sensitive to the increase in temperature leading to ignition.

6 The relatively large sensitivity coefficient of H-atom abstraction from primary carbon atoms
7 indicates the branching ratio of this reaction class is also important in controlling reactivity. As
8 discussed above, H-atom abstraction occurs preferentially from secondary carbon atoms. However, the
9 concerted elimination reaction that inhibits reactivity also favors secondary alkylperoxy radicals, since
10 there are more hydrogen atoms on beta carbons. On the other hand, primary alkylperoxy radicals,
11 C₇H₁₅-1 \dot{O} ₂, only have two hydrogen atoms on the beta carbon leading to the concerted elimination
12 reaction, and therefore there is less competition from this reaction class in the sequent chain branching
13 process. Besides H₂/O₂ and C₁ chemistry, the reactions of other small molecules also become sensitive.
14 For example, the concerted elimination of *n*-propyl peroxide radical (*n*C₃H₇ \dot{O} ₂) inhibits reactivity.
15 These small molecule radicals are mainly produced from the β -scission of fuel-derived radicals or from
16 low-temperature products of the chain branching process.

17 The chemistry of small molecule species is even more important in the high-temperature regime,
18 as shown in Fig. 9 (c). As the temperature increases, the decomposition of H₂O₂ is further enhanced and
19 becomes the dominant reaction promoting reactivity. Correspondingly, H-atom abstraction from fuel by
20 HO₂ radicals, which converts HO₂ radicals into H₂O₂, greatly promotes reactivity. On the other hand,
21 the duplicated chain terminating reactions of HO₂ radicals are the most inhibiting reactions, as
22 discussed above. The unimolecular decomposition of the fuel and β -scission of the fuel-derived radicals
23 show positive or negative sensitivity coefficients depending on the reactivity of the different smaller
24 hydrocarbon species produced. The low-temperature chain branching reactions are not observed to be
25 sensitive in Fig 9 (c) due to the high temperature conditions. A series of reactions between small
26 molecule hydrocarbon radicals and HO₂ radicals are shown in Fig. 9 (c). In general, those converting
27 HO₂ into $\dot{O}H$ radicals directly or indirectly promote reactivity, while those converting HO₂ into O₂
28 inhibit reactivity.

29 *Jet stirred reactor*

30 The jet-stirred reactor experiments were performed at 1.06 bar, at a residence time of 2s and at
31 equivalence ratios of 0.25, 2.0 and 4.0 in order to extend the relevant experimental database to very lean
32 ($\varphi = 0.25$) and very rich ($\varphi = 4.0$) conditions. Detailed compositions of the mixtures are listed in Table 3,
33 with over 40 species being identified. The intermediates include C₁-C₂ alcohols, C₁-C₄ aldehydes, C₁-
34 C₄ alkanes, C₂-C₇ alkenes, small molecular dienes and alkynes, C₇ cyclic ethers, as well as other
35 oxygenated species such as acids and unsaturated aldehydes, which can be produced from the low-
36 temperature oxidation process. The simulation has been performed using the perfectly-stirred reactor

1 module within CHEMKIN PRO [84] employing the transient solver, with an end-time of 20 s. Figures
2 10–12 present the model versus experimental results at equivalence ratios of 0.25, 2.0 and 4.0,
3 respectively. The experimental data sets are available in the supplementary material.

4 The NTC behavior of *n*-heptane under different conditions is reflected in the experimental
5 results. In general, the experimental trends are well captured by the model, except for the under-
6 prediction in reactivity at $\varphi = 0.25$ at a temperature of approximately 750 K, indicating that the current
7 mechanism can capture the overall chemical behavior of *n*-heptane under most conditions studied in the
8 present work. Good agreement is observed between the experimental results and the predictions for
9 major intermediates, with the deviations in the peak concentrations being mostly within a factor of two
10 of the experiments. However, the deviations for oxygenated species at low temperatures, such as those
11 shown in Fig 10 (j), Fig 11 (b) and Fig 11 (f), suggest that the consumption pathway of the low-
12 temperature chemistry products can be further refined. In the current mechanism, the Korcek
13 mechanism [87] which produces acids from ketohydroperoxides has also been considered, with the rate
14 constants adopted from Pelucchi *et al.* [44]. However, the effects of adopting this reaction class are very
15 slight, as the concentrations of the acids are under-predicted at all conditions studied in this work,
16 especially for the leanest mixture which requires further investigation. This might be due to the fast
17 decomposition of ketohydroperoxides in the current model which requires further investigation of the
18 detailed reaction pathways that consume ketohydroperoxides. The dashed lines present the simulations
19 using the mechanism with unmodified rate rules. It can be seen that the new modifications have only a
20 slight effect upon the predicted mole fraction profiles of major species. The dashed lines are
21 overlapping with the solid lines for many cases.

22 It is worth noting that two important classes of intermediates are reasonably well predicted by the
23 model, that is, heptenes and C_7 cyclic ethers. As shown in Fig 10–12 (m), the heptene isomers are
24 largely produced from the concerted elimination reactions of RO_2 radicals, to which ignition delay
25 times are sensitive, showing different effects depending on the temperature range, as discussed earlier.
26 The overall agreement between the model and experimental results of 1-, 2- and 3-heptene are better
27 predicted using the modified rate rules adopted here, yet the branching ratio may need to be further
28 refined. Another possible reason for the deviations, especially those at intermediate temperatures, may
29 be attributable to the consumption pathways of these alkenes. The experimental and simulated mole
30 fraction profiles of five different C_7 cyclic ethers are shown in Figs. 10–12 (n)–(o). These species are
31 produced from the chain propagating reactions of $QOOH$ radicals forming cyclic ethers and $\dot{O}H$
32 radicals. Although this reaction class is not seen to be sensitive according to our analysis presented
33 above, its significance for the consumption of RO_2 radicals cannot be neglected, as will be shown in the
34 rate of production analysis below. Using the modified rate rules adopted here, in general the predicted
35 mole fraction profiles agree better with the experimental results. Even at $\varphi = 0.25$, where the
36 performance of the model is not as good as at the other equivalence ratios, the predicted peak
37 concentration of cyclic ethers match the magnitude of the measured values.

1 Figures 13 and 14 present the validation of the model against experimental data from previous
2 studies [16-17] in the same jet-stirred reactor. The experimental conditions are similar having a fuel
3 concentration of 0.5% using helium as the diluent gas. The pressure was 1.06 bar with the residence
4 time of 2s. The equivalence ratios were 1.0 and 3.0, respectively. The agreement of the predicted mole
5 fraction profiles with the measured ones is good for the major species. Figures 13 (d) and Fig. 13 (f)
6 show the mole fraction profiles of cyclic ethers and the heptene isomers. The cyclic ethers are well-
7 predicted, while the heptenes are over-predicted within a factor of two. Similar trends are seen in Fig.
8 14 (d) for the $\phi = 3.0$ condition, as the concentrations of the two cyclic ethers are well predicted, while
9 the agreement for 1- and 2-heptene shown in Fig. 14 (f), are better than those at the stoichiometric
10 condition. However, certain deviations are observed at low temperatures for oxygenated species at $\phi =$
11 3.0, such as acetaldehyde and propanal shown in Fig 14 (c) and (e). Figure 15 shows the validations at
12 higher pressures, which uses the experimental data from Dagaut et al. [14]. The model can in general
13 reproduce well the species mole fraction profiles. The predicted mole fraction profiles of the heptane
14 isomers agree better with the experimental results as shown in Fig. 15 (f) compared to those at 1.06 bar,
15 while certain deviations between the experimental and modeling results can be observed for some
16 smaller alkenes such as ethylene and propene as shown in Fig. 15 (b) and Fig. 15 (c). These
17 observations indicate that the consumption pathways for the primary oxidation products of *n*-heptane
18 may need further refinement, possibly by firstly considering their pressure dependence.

19 Simulations have also been performed using the mechanisms proposed by Mehl *et al.* [42],
20 Herbinet *et al.* [16], Pelucchi *et al.* [44] Seidel *et al.* [30] and Cai *et al.* [46] and compared with those of
21 the current mechanism. The experimental data sets are taken from [16]. Comparisons are shown in Fig.
22 16, with each row comparing the simulated results using the current mechanism compared to the target
23 mechanism, which indicates that the current mechanism has an overall better performance. Rate of
24 production analyses have been performed for *n*-heptane oxidation in the jet-stirred reactor using helium
25 diluted at 0.5% fuel, at a residence time of 2 s, at $\phi = 1$, and at $T = 650, 850$ and 1000 K in order to
26 reflect the significant reaction pathways over the entire temperature range. Based on the results at the
27 three different temperatures, a reaction pathway diagram has been generated following two principles
28 and is shown in Fig. 17. Considering the neatness of the diagram, the first principle is that, the reaction
29 pathways with contributions of less than 10% at all three temperatures are not shown. Some of the
30 remaining pathways may have very low contributions at either low or high temperatures due to their
31 dependence on temperature; e.g. the addition of fuel derived radicals to oxygen. Therefore the second
32 principle is that, if a reaction pathway has a contribution of less than 6%, the contributions of the
33 sequent reaction pathways of its product are not shown. The arrows denote reaction pathways, with
34 their contributions under different temperatures indicated using different fonts: red italic denotes $T =$
35 650 K, black bold denotes $T = 850$ K and blue underlined denotes $T = 1000$ K.

36 At all three temperatures, fuel consumption occurs mainly via H-atom abstraction by the radical
37 pool, with a slight change in the branching ratios leading to different fuel derived radicals (\dot{R}). An

1 analysis of the branching ratio for abstraction by different radicals indicates that the contribution of H-
2 atom abstraction by $\dot{\text{O}}\text{H}$ radicals to fuel consumption is 95.8% at 650 K, 78.1% at 850 K and 43.5% at
3 1000 K, while that by $\dot{\text{H}}$ atoms is 3.1% at 650 K, 9.1% at 850 K and 52.7% at 1000 K. This reflects the
4 inhibited chain propagating process due to increasing temperature, as well as the enhanced β -scission of
5 fuel derived radicals which readily produce $\dot{\text{H}}$ atoms in the sequent dehydrogenation reactions. This
6 overall trend can also be observed from the change in flux distribution with increasing temperature.
7 Unlike those of $\dot{\text{O}}\text{H}$ radicals and $\dot{\text{H}}$ atoms, the contributions to fuel consumption of H-atom abstraction
8 by $\dot{\text{H}}\text{O}_2$ radical is 0.7% at 650 K, 9.1% at 850 K and 2.2% at 1000 K. This trend is consistent with the
9 discussions on sensitivity analysis for ignition delay time in that H-atom abstraction from the fuel by
10 $\dot{\text{H}}\text{O}_2$ radicals plays an important role at intermediate temperatures (~ 850 – 1300 K). The production of $\dot{\text{R}}$
11 radicals is depicted in the upper left part of Fig. 17, and the consumption is shown in the order of 1-, 2-,
12 3- and 4-heptyl vertically. In general, the chain propagation and chain branching processes in the
13 consumption of each fuel radical are depicted from left to right in Fig.17; the left edge shows the
14 reaction classes such as the β -scission and isomerization reactions of alkyl radicals, followed by chain
15 propagation reactions including the addition of alkyl radicals to O_2 , concerted elimination of $\text{R}\dot{\text{O}}_2$
16 radicals producing an $\dot{\text{H}}\text{O}_2$ radical and an olefin, which competes with the isomerization of $\text{R}\dot{\text{O}}_2$ into
17 $\dot{\text{Q}}\text{OOH}$ radicals. In the middle part of Fig.17, the multiple consumption channels of $\dot{\text{Q}}\text{OOH}$ are shown,
18 including $\dot{\text{Q}}\text{OOH}$ radical addition to O_2 , the formation of cyclic ethers and also the β -scission reactions
19 producing smaller molecule products. On the right edge, the chain branching step is reached via the
20 formation of ketohydroperoxide species and bi-hydroperoxy alkyl radicals. The formation and
21 decomposition of the former produce two $\dot{\text{O}}\text{H}$ radicals in total, while the decomposition of the latter
22 also releases two $\dot{\text{O}}\text{H}$ radicals. The further decomposition pathways of these species are not depicted
23 here in order to reduce the size of the figure. Alternative isomerization reactions are more important for
24 O_2QOOH radicals where the hydroperoxy groups are on primary carbon atoms. This is because the C–
25 H bonds are stronger and are not favored by the internal H-atom transfer process. Although for *n*-
26 heptane, the alternative isomerization reaction leads to chain branching which can also be reached via
27 the formation of ketohydroperoxides, this additional pathway may be important for branched alkanes
28 when the formation of ketohydroperoxides is not possible [51].

29 At 650 K, the chain branching process dominates, with the production of ketohydroperoxides and
30 bi-hydroperoxyl alkyl radicals at the right end of Fig.17. The β -scission pathway of each fuel derived
31 radical can be neglected. The concerted elimination reactions of $\text{R}\dot{\text{O}}_2$ have lesser contributions
32 compared to those of the isomerization into $\dot{\text{Q}}\text{OOH}$ radicals. However, ignition delay time predictions
33 are very sensitive to these concerted elimination reactions where an increase in their rate reduces
34 reactivity, as shown in Fig 9. On the other hand, the flux leading to cyclic ethers is quite high. For each
35 $\text{R}\dot{\text{O}}_2$ radical, the 1,4 H-atom transfer channel is favored over the other isomerization pathways, and the
36 sequent formation of five membered ring cyclic ethers dominates the consumption of the corresponding
37 $\dot{\text{Q}}\text{OOH}$ radicals. However, the reactivity of the system is in-sensitive to the formation of cyclic ethers

1 because these chain propagation reactions produce $\dot{\text{O}}\text{H}$ radicals which are much more reactive than the
2 $\text{H}\dot{\text{O}}_2$ radicals produced from the concerted elimination reactions of $\text{R}\dot{\text{O}}_2$ radicals at low temperatures. As
3 the temperature increases to 850 K, the chain propagation pathways become more dominant and there is
4 little flux to chain branching and $\dot{\text{Q}}\text{OOH}$ radical addition to O_2 . An obvious feature in the reaction
5 pathways is that the concerted elimination reactions largely consume $\text{R}\dot{\text{O}}_2$ radicals, especially secondary
6 $\text{R}\dot{\text{O}}_2$ radicals since there are more hydrogen atoms on the beta carbons. Meanwhile, the formation of
7 cyclic ethers is also enhanced. As has been discussed previously, the production of 1-heptyl radicals
8 promotes reactivity, with this class of reaction showing a relatively large sensitivity coefficient at
9 intermediate temperatures. This may be partly explained by the consumption channels of different fuel
10 radicals shown in Fig. 17. While the concerted elimination reaction dominates the consumption of 2-, 3-
11 and 4-heptyl radicals, the isomerization reactions contribute about 69% in total to the consumption of 1-
12 heptyl radicals. Therefore the production of 1-heptyl radicals, compared to the other heptyl radicals,
13 increases the chain branching process, and thus promotes reactivity. At the higher temperature condition
14 of 1000 K, the only important consumption pathways for alkyl radicals are β -scissions, simultaneously
15 producing smaller hydrocarbon radicals and olefins. Therefore the chemistry of these smaller
16 hydrocarbon species becomes important in controlling the reactivity of the system. The addition of alkyl
17 radicals to molecular oxygen has only a minor contribution to the overall flux of the system.

18 Rate of production analyses have also been performed at $\varphi = 0.25$ and $\varphi = 4.0$ at $T = 650$ K to
19 determine the influence of equivalence ratio upon the oxidation of *n*-heptane through the reaction
20 pathways shown in Fig. 17. The contributions have been marked with numbers in red frames and
21 numbers with red backgrounds for $\varphi = 0.25$ and $\varphi = 4.0$ at $T = 650$ K, respectively. As shown by the
22 experimental conditions in Table 3, the concentration of the fuel remains constant, while that of oxygen
23 varies with increasing equivalence ratio. As a result, the reactions involving oxygen are enhanced at $\varphi =$
24 0.25 and inhibited at $\varphi = 4.0$. This is reflected in Fig. 17 in that the additions of $\dot{\text{R}}$ and $\dot{\text{Q}}\text{OOH}$ radicals
25 to molecular oxygen, especially the latter, have higher contributions at the fuel-lean condition. For
26 example, the addition of $\text{C}_7\text{H}_{14}\text{OOH}_{4-2}$ radicals to oxygen account for 89.2%, 67.2% and 35.5% to its
27 consumption at $\varphi = 0.25$, 1.0, and 4.0, respectively, shown at the bottom of Fig. 17. For the
28 consumption of $\dot{\text{Q}}\text{OOH}$ radicals, the lower contribution of the addition to O_2 with an increase in
29 equivalence ratio leads directly to the higher contribution of cyclic ether formation. Meanwhile, the
30 equilibrium between $\text{R}\dot{\text{O}}_2$ and $\dot{\text{Q}}\text{OOH}$ radicals is also affected. As the consumption of $\dot{\text{Q}}\text{OOH}$ radicals is
31 actually inhibited by the lack of O_2 at the fuel-rich condition, the isomerization of $\dot{\text{Q}}\text{OOH}$ radicals back
32 to $\text{R}\dot{\text{O}}_2$ radicals and the consumption of $\text{R}\dot{\text{O}}_2$ radicals via other reaction pathways are promoted. Figure
33 17 shows that the production of 3-heptene from $\text{C}_7\text{H}_{15-4}\dot{\text{O}}_2$ radical contribute 15.3%, 32.9% and 45.7%
34 to its consumption at $\varphi = 0.25$, 1.0, and 4.0, respectively. According to the results and discussions of the
35 sensitivity analysis shown in Fig. 9, these changes lead to a lower reactivity at fuel-rich conditions,
36 which is consistent with the fuel consumption values shown in Figs. 10–12 (b). On the other hand, the
37 branching ratios in the production of different fuel derived radicals are very similar at all of the three

1 equivalence ratios. This is because H-atom abstraction from the fuel occurs mainly via $\dot{\text{O}}\text{H}$ radicals,
2 with only minor contributions from the other radicals, but varies with equivalence ratio. Similarly, the
3 branching ratios of different consumption channels of $\dot{\text{O}}_2\text{QOOH}$ radicals are also highly consistent
4 despite of the varying equivalence ratio, since they are mainly consumed via isomerization and sequent
5 decomposition.

6 *Laminar flame speed predictions*

7 The current mechanism has been validated using the laminar flame speed data reported in [24-26].
8 The comparisons are shown in Figs. 18–20. The simulation used the premix code in CHEMKIN PRO
9 [84]. Considering the high temperature condition in the flame, the current mechanism has been reduced
10 by removing most of the reactions involving low-temperature species. This reduced mechanism, or the
11 high temperature version of the current mechanism, is also available as Supplementary material and at
12 the C₃ website: <http://c3.nuigalway.ie/>.

13 Dirrenberger *et al.* measured adiabatic laminar burning velocities of *n*-heptane at 1 atm using a
14 flat flame adiabatic burner [26]. The heat flux method was used to determine burning velocities at
15 conditions for which the net heat loss of the flame is zero. Figure 18 shows the experimental data sets
16 reported for *n*-heptane flame speeds, which were measured at 298 K, 358 K and 398 K [26]. The model
17 predicts well the flame speeds except for the under-prediction at fuel-rich conditions, which is similar to
18 the deviations between the experimental and modeling results presented in the original paper [26].
19 Sileghem *et al.* measured the laminar burning velocities of *n*-heptane using the heat flux method for a
20 flat flame adiabatic burner at atmospheric pressure and at multiple initial temperatures from 298 K to
21 358 K [25]. Good agreement can be seen between the experimental data and the simulations using the
22 current model for all data sets at initial temperature from 298 K to 358 K (Fig. 19). Only slight under-
23 predictions can be seen at the initial temperature of 358 K. The deviations are mostly within the
24 reported uncertainty range (± 1.4 cm/s for equivalence ratio = 1.3 and ± 1 cm/s for the other equivalence
25 ratios).

26 The current mechanism has been further validated against flame speed data at elevated pressures.
27 Kelly *et al.* performed experimental study on laminar flame speeds and Markstein lengths studies for
28 C₅–C₈ *n*-alkane mixtures in air at pressures of up to 10 atm [24]. Figure 20 shows the measured *n*-
29 heptane flame speeds at an initial temperature of 353 K and at pressures of 1, 2, 5, and 10 atm,
30 respectively. The predicted flame speeds agree well with the experimental results at all pressures, with
31 slight under-predictions at 5 atm which are within the reported uncertainty range of ± 2 cm/s. This
32 indicates that the pressure dependence of the high temperature chemistry is reasonable in the current
33 mechanism.

34

1 **Conclusions**

2 In this work, the oxidation of *n*-heptane has been firstly investigated experimentally. A detailed
3 chemical kinetic model has been developed to numerically describe these experimental observations.
4 Good agreement is observed between the model predictions and measured ignition delay times. In
5 general, the model also satisfactorily captures the trend in the mole fraction profiles of most species
6 measured in a jet-stirred reactor over a very wide range of equivalence ratios (0.25, 2.0 and 4.0). A
7 good performance of the current mechanism is also indicated via further validations and comparisons to
8 several recently published *n*-heptane mechanisms. The reaction rate rules used in this mechanism are
9 consistent with those used for the pentane isomers [51, 55] and *n*-hexane [54] sub-mechanisms.
10 Therefore good consistency in kinetic can be expected, which is important regarding simulations for
11 fuel mixtures. The reaction rate rules have been shown to lead to reasonably good predictions and may
12 thus be used in the development of mechanisms of larger alkanes.

13 **Acknowledgments**

14 At NUIG, the research leading to these results has received funding from the People Programme
15 (Marie Curie Actions) of the European Union's Seventh Framework Programme FP7/2007-2013/ under
16 REA grant agreement n° 607214. At LRGP, this work was supported by COST Action CM1404. At
17 PCFC, the authors acknowledge the support of the cluster of excellence “Tailor Made Fuels from
18 Biomass” for the work at PCFC, which is funded by the Excellence Initiative by the German federal
19 and state governments to promote science and research at German universities.

1 **References**

- 2 [1] Samimi-Abianeh, O., *J. Eng. Gas Turbines Power*, **2015**, *137*, GTP-14-1320.
- 3 [2] Curran, H. J., Pitz, W. J., Westbrook, C. K., Callahan, C. V., and Dryer, F. L., *Proc.*
4 *Combust. Inst.*, **1998**, *27*, 379-387.
- 5 [3] Vermeer, D. J., Meyer, J. W., and Oppenheim, A. K., *Combust. Flame*, **1972**, *18*, 327-
6 336.
- 7 [4] Coats, C. M. and Williams, A., *Proc. Combust. Inst.*, **1979**, *17*, 611-621.
- 8 [5] Ciezki, H. and Adomeit, G., *Combust. Flame*, **1993**, *93*, 421-433.
- 9 [6] Herzler, J., Jerig, L., and Roth, P., *Proc. Combust. Inst.*, **2005**, *30*, 1147-1153.
- 10 [7] Davidson, D. F., Hong, Z., Pilla, G. L., Farooq, A., Cook, R. D., and Hanson, R. K.,
11 *Combust. Flame*, **2010**, *157*, 1899-1905.
- 12 [8] Zhang, J., Niu, S., Zhang, Y., Tang, C., Jiang, X., Hu, E., and Huang, Z., *Combust.*
13 *Flame*, **2013**, *160*, 31-39.
- 14 [9] Griffiths, J. F., Hughes, K. J., Schreiber, M., and Poppe, C., *Combust. Flame*, **1994**, *99*,
15 533-540.
- 16 [10] Minetti, R., Carlier, M., Ribaucour, M., Therssen, E., and Sochet, L. R., *Combust.*
17 *Flame*, **1995**, *102*, 298-309.
- 18 [11] Cox, A., Griffiths, J. F., Mohamed, C., Curran, H. J., Pitz, W. J., and Westbrook, C. K.,
19 *Proc. Combust. Inst.*, **1996**, *26*, 2685-2692.
- 20 [12] Silke, E. J., Curran, H. J., and Simmie, J. M., *Proc. Combust. Inst.*, **2005**, *30*, 2639-
21 2647.
- 22 [13] Chakir, A., Bellimam, M., Boettner, J. C., and Cathonnet, M., *Int. J. Chem. Kinet.*,
23 **1992**, *24*, 385-410.
- 24 [14] Dagaut, P., Reuillon, M., and Cathonnet, M., *Combust. Sci. Technol.*, **1993**, *95*, 233-
25 260.
- 26 [15] Dagaut, P., Reuillon, M., and Cathonnet, M., *Combust. Flame*, **1995**, *101*, 132-140.
- 27 [16] Herbinet, O., Husson, B., Serinyel, Z., Cord, M., Warth, V., Fournet, R., Glaude, P.-A.,
28 Sirjean, B., Battin-Leclerc, F., Wang, Z., Xie, M., Cheng, Z., and Qi, F., *Combustion*
29 *and Flame*, **2012**, *159*, 3455-3471.
- 30 [17] Hakka, H. M., Cracknell, R. F., Pekalski, A., Glaude, P. A., and Battin-Leclerc, F., *Fuel*,
31 **2015**, *144*, 358-368.
- 32 [18] Callahan, C. V., Held, T. J., Dryer, F. L., Minetti, R., Ribaucour, M., Sochet, L. R.,
33 Faravelli, T., Gaffuri, P., and Rani, E., *Proc. Combust. Inst.*, **1996**, *26*, 739-746.
- 34 [19] Held, T., Marchese, A., and Dryer, F., *Combust. Sci. Technol.*, **1997**, *123*, 107-146.

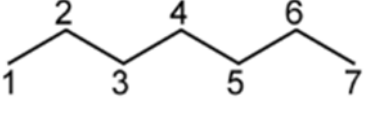
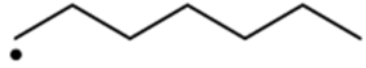
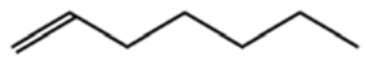
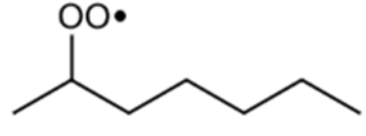
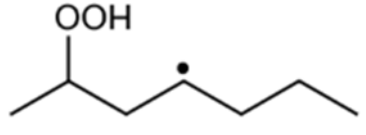
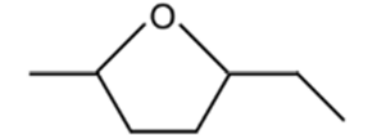
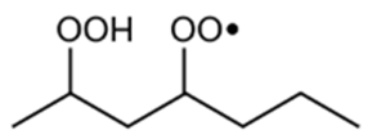
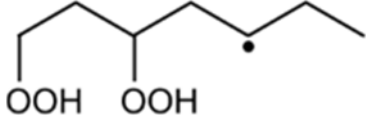
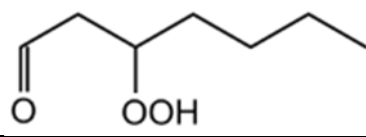
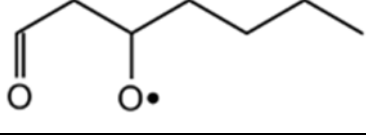
- 1 [20] Lenhert, D. B., Miller, D. L., Cernansky, N. P., and Owens, K. G., *Combust. Flame*,
2 **2009**, *156*, 549-564.
- 3 [21] Veloo, P., Jahangirian, S., and Dryer, F., Proceedings of the Spring Technical Meeting
4 of the Central States Section of the Combustion Institute; Dayton, OH, April 22–24,
5 2012.
- 6 [22] Smallbone, A. J., Liu, W., Law, C. K., You, X. Q., and Wang, H., *Proc. Combust. Inst.*,
7 **2009**, *32*, 1245-1252.
- 8 [23] Ji, C., Dames, E., Wang, Y. L., Wang, H., and Egolfopoulos, F. N., *Combust. Flame*,
9 **2010**, *157*, 277-287.
- 10 [24] Kelley, A. P., Smallbone, A. J., Zhu, D. L., and Law, C. K., *Proc. Combust. Inst.*, **2011**,
11 *33*, 963–970.
- 12 [25] Sileghem, L., Alekseev, V. A., Vancoillie, J., Geem, K. M. V., Nilsson, E. J. K.,
13 Verhelst, S., and b, A. A. K., *Fuel*, **2013**, *112*, 355-365.
- 14 [26] Dirrenberger, P., Glaude, P. A., Bounaceur, R., Gall, H. L., Cruz, A. P. d., Konnov, A.
15 A., and Battin-Leclerc, F., *Fuel*, **2014**, *115*, 162-169.
- 16 [27] Yao, C., Cheng, C., Liu, S., Tian, Z., and Wang, J., *Fuel*, **2009**, *88*, 1752-1757.
- 17 [28] Song, J., Yao, C., Liu, S., Tian, Z., and Wang, J., *Fuel*, **2009**, *88*, 2297-2302.
- 18 [29] Chen, G., Yu, W., Fu, J., Mo, J., Huang, Z., Yang, J., Wang, Z., Jin, H., and Qi, F.,
19 *Combust. Flame*, **2012**, *159*, 2324-2335.
- 20 [30] Seidel, L., Moshhammer, K., Wang, X., Zeuch, T., Kohse-Höinghaus, K., and Mauss, F.,
21 *Combust. Flame*, **2015**, *162*, 2045-2058.
- 22 [31] Cavaliere, A., Ciajolo, A., D'Anna, A., Mercogliano, R., and Ragucci, R., *Combust.*
23 *Flame*, **1993**, *93*, 279-286.
- 24 [32] Kim, D. S. and Lee, C. S., *Fuel*, **2006**, *85*, 695-704.
- 25 [33] Lu, X. C., Chen, W., and Huang, Z., *Fuel*, **2005**, *84*, 1074–1083.
- 26 [34] Lu, X. C., Chen, W., and Huang, Z., *Fuel*, **2005**, *84*, 1084–1092.
- 27 [35] Szybist, J. P., Boehman, A. L., Haworth, D. C., and Koga, H., *Combust. Flame*, **2007**,
28 *149*, 112-128.
- 29 [36] Westbrook, C. K., Warnatz, J., and Pitz, W. J., *Proc. Combust. Inst.*, **1989**, *22*, 893-901.
- 30 [37] Chevalier, C., Pitz, W. J., Warnatz, J., Westbrook, C. K., and Melenk, H., *Proc.*
31 *Combust. Inst.*, **1992**, *24*, 93-101.
- 32 [38] Ranzi, E., Gaffuri, P., Faravelli, T., and Dagaut, P., *Combust. Flame*, **1995**, *103*, 91-106.
- 33 [39] Côme, G. M., Warth, V., Glaude, P. A., Fournet, R., Battin-Leclerc, F., and Scacchi, G.,
34 *Proc. Combust. Inst.*, **1996**, *26*, 755-762.

- 1 [40] Curran, H. J., Gaffuri, P., Pitz, W. J., and Westbrook, C. K., *Combust. Flame*, **1998**,
2 *114*, 149-177.
- 3 [41] Westbrook, C. K., Pitz, W. J., Herbinet, O., Curran, H. J., and Silke, E. J., *Combust.*
4 *Flame*, **2009**, *156*, 181-199.
- 5 [42] Mehl, M., Pitz, W. J., Westbrook, C. K., and Curran, H. J., *Proc. Combust. Inst.*, **2011**,
6 *33*, 193-200.
- 7 [43] Biet, J., Hakka, M. H., Warth, V., Glaude, P. A., and Battin-Leclerc, F., *Energy Fuels*,
8 **2008**, *22*, 2258-2269.
- 9 [44] Pelucchi, M., Bissoli, M., Cavallotti, C., Cuoci, A., Faravelli, T., Frassoldati, A., Ranzi,
10 E., and Stagni, A., *Energy Fuels*, **2014**, *28*, 7178-7193.
- 11 [45] Shen, H.-P. S., Steinberg, J., Vanderover, J., and Oehlschlaeger, M. A., *Energy Fuels*,
12 **2009**, *23*, 2482-2489.
- 13 [46] Cai, L. and Pitsch, H., *Combustion and Flame*, **2015**, *162*, 1623-1637.
- 14 [47] Metcalfe, W. K., Burke, S. M., Ahmed, S. S., and Curran, H. J., *Int. J. Chem. Kinet.*,
15 **2013**, *45*, 638-675.
- 16 [48] Kéromnès, A., Metcalfe, W. K., Heufer, K. A., Donohoe, N., Das, A. K., Sung, C.-J.,
17 Herzler, J., Naumann, C., Griebel, P., Mathieu, O., Krejci, M. C., Petersen, E., Pitz, W.
18 J., and Curran, H. J., *Combust. Flame*, **2013**, *160*, 995-1011.
- 19 [49] Burke, S. M., Metcalfe, W. K., Herbinet, O., Battin-Leclerc, F., Haas, F. M., Santner, J.,
20 Dryer, F. L., and Curran, H. J., *Combust. Flame*, **2014**, *161*, 2765-2784.
- 21 [50] Burke, S. M., Burke, U., Donagh, R. M., Mathieu, O., Osorio, I., Keesee, C., Morones,
22 A., Petersen, E. L., Wang, W., DeVerter, T. A., Oehlschlaeger, M. A., Rhodes, B.,
23 Hanson, R. K., Davidson, D., Weber, B. W., Sung, C.-J., Santner, J., Ju, Y., Haas, F. M.,
24 Dryer, F. L., Volkov, E. N., Nilsson, E. J. K., Konnov, A. A., Alrefae, M., Khaled, F.,
25 Farooq, A., Dirrenberger, P., Glaude, P.-A., Battin-Leclerc, F., and Curran, H. J.,
26 *Combust. Flame*, **2015**, *162*, 296-314.
- 27 [51] Bugler, J., Somers, K. P., Silke, E. J., and Curran, H. J., *J. Phys. Chem. A*, **2015**, *119*,
28 7510-7527.
- 29 [52] Burke, S. M., Simmie, J. M., and Curran, H. J., *J. Phys. Chem. Ref. Data*, **2015**, *44*,
30 013101.
- 31 [53] Burke, U., Somers, K. P., O'Toole, P., Zinner, C. M., Marquet, N., Bourque, G.,
32 Petersen, E. L., Metcalfe, W. K., Serinyel, Z., and Curran, H. J., *Combust. Flame*, **2015**,
33 *162*, 315-330.
- 34 [54] Zhang, K., Banyon, C., Togbé, C., Dagaut, P., Bugler, J., and Curran, H. J., *Combust.*
35 *Flame*, **2015**, *162*, 4194-4207.
- 36 [55] Bugler, J., Marks, B., Mathieu, O., Archuleta, R., Camou, A., Grégoire, C., Heufer, K.
37 A., Petersen, E. L., and Curran, H. J., *Combust. Flame*, **2016**, *163*, 136-156.

- 1 [56] Burke, U., Metcalfe, W. K., Burke, S. M., Heufer, K. A., Dagaut, P., and Curran, H. J.,
2 *Combust. Flame*, **2016**, *in press*,
- 3 [57] Li, Y., Zhou, C. W., Somers, K. P., Zhang, K., and Curran, H. J., *Proc. Combust. Inst.*,
4 **2016**, *submitted*,
- 5 [58] Zhou, C. W., Li, Y., O'Connor, E., Somers, K. P., Thion, S., Keesee, C., Mathieu, O.,
6 Petersen, E. L., DeVerter, T. A., Oehlschlaeger, M. A., Kukkadapu, G., Sung, C.-J.,
7 Alrefae, M., Khaled, F., Farooq, A., Dirrenberger, P., Glaude, P.-A., Battin-Leclerc, F.,
8 Santner, J., Ju, Y., Held, T., Haas, F. M., Dryer, F. L., and Curran, H. J., *Combust.*
9 *Flame*, **2016**, *accepted*,
- 10 [59] *Shock and detonation toolbox*,
11 http://shepherd.caltech.edu/EDL/public/cantera/html/SD_Toolbox/, accessed: 2015-11-
12 25,
- 13 [60] Goodwin, D. G., Moat, H. K., and Speth, R. L., *Cantera: An object-oriented software*
14 *toolkit for chemical kinetics, thermodynamics, and transport processes*,
15 <http://www.cantera.org>, version 2.2.0 (2015),
- 16 [61] Nakamura, H., Darcy, D., Mehl, M., Tobin, C. J., Metcalfe, W. K., Pitz, W. J.,
17 Westbrook, C. K., and Curran, H. J., *Combust. Flame*, **2014**, *161*, 49-64.
- 18 [62] Matras, D. and Villermaux, J., *Chem. Eng. Sci.*, **1973**, *28*, 129-137.
- 19 [63] Herbinet, O. and Battin-Leclerc, F., *Int. J. Chem. Kinet.*, **2014**, *46*, 619-639.
- 20 [64] Andreatch, A. and Feinland, R., *Anal. Chem.*, **1960**, *32*, 1021-1024.
- 21 [65] Dietz, W., *J. Gas Chromatogr.*, **1967**, *5*, 68-71.
- 22 [66] The National Institute of Standards and Technology, June 19, 2014,
23 <<http://www.nist.gov/srd/nist1a.cfm>>.
- 24 [67] Rodriguez, A., Herbinet, O., Wang, Z., Qi, F., Fittschen, C., Westmoreland, P., and
25 Battin-Leclerc, F., *Proceedings of the Combustion Institute*, **2016**, *36*, Accepted.
- 26 [68] Sharma, S., Raman, S., and Green, W. H., *J. Phys. Chem. A*, **2010**, *114*, 5689-5701.
- 27 [69] Miyoshi, A., *Int. J. Chem. Kinet.*, **2012**, *44*, 59-74.
- 28 [70] Goldsmith, C. F., Green, W. H., and Klippenstein, S. J., *J. Phys. Chem. A*, **2012**, *116*,
29 3325-3346.
- 30 [71] Villano, S. M., Huynh, L. K., Carstensen, H.-H., and Dean, A. M., *J. Phys. Chem. A*,
31 **2011**, *115*, 13425-13442.
- 32 [72] Villano, S. M., Huynh, L. K., Carstensen, H.-H., and Dean, A. M., *J. Phys. Chem. A*,
33 **2012**, *116*, 5068-5089.
- 34 [73] Villano, S. M., Carstensen, H.-H., and Dean, A. M., *J. Phys. Chem. A*, **2013**, *117*, 6458-
35 6473.

- 1 [74] Ritter, E. R. and Bozzelli, J. W., *Int. J. Chem. Kinet.*, **1991**, *23*, 767-778.
- 2 [75] Benson, S. W., *Thermochemical Kinetics*, 2nd ed., Wiley: New York, 1976.
- 3 [76] Rolland, S. and Simmie, J. M., *Int. J. Chem. Kinet.*, **2005**, *37*, 119-125.
- 4 [77] Pelucchi, M., Somers, K. P., Yasunaga, K., Burke, U., Frassoldati, A., Ranzi, E.,
5 Curran, H. J., and Faravelli, T., *Combust. Flame*, **2015**, *162*, 265-286.
- 6 [78] Jasper, A. W. and Miller, J. A., *Combust. Flame*, **2014**, *161*, 101-110.
- 7 [79] Tsang, W., Awan, I. A., McGivern, W. S., and Manion, J. A., "*Soot precursor from real*
8 *fuels: the unimolecular reaction of fuel radicals*" in *Combustion Generated Fine*
9 *Carbonaceous Particles*, Proceedings of an International Workshop held in Villa
10 Orlandi, Anacapri, May 13-16, 2007 ed. vol. ISBN: 978-3-86644-441-6: KIT Scientific
11 Publishing, 2009.
- 12 [80] Sivaramakrishnan, R. and Michael, J. V., *J. Phys. Chem. A*, **2009**, *113*, 5047-5060.
- 13 [81] Aguilera-Iparraguirre, J., Curran, H. J., Klopper, W., and Simmie, J. M., *J. Phys. Chem.*
14 *A*, **2008**, *112*, 7047-7054.
- 15 [82] Heufer, K. A. and Olivier, H., *Shock Waves*, **2010**, *20*, 307-316.
- 16 [83] Gauthier, B. M., Davidson, D. F., and Hanson, R. K., *Combustion and Flame*, **2004**,
17 *139*, 300-311.
- 18 [84] *CHEMKIN-PRO 15101, Reaction Design, San Diego, 2010.*,
- 19 [85] Petersen, E. L. and Hanson, R. K., *Shock Waves*, **2001**, *10*, 405-420.
- 20 [86] Campbell, M. F., Wang, S., Goldenstein, C. S., Spearrin, R. M., Tulgestke, A. M.,
21 Zaczek, L. T., Davidson, D. F., and Hanson, R. K., *Proc. Combust. Inst.*, **2015**, *35*, 231-
22 239.
- 23 [87] Jalan, A., Alecu, I. M., Meana-Pañeda, R., Aguilera-Iparraguirre, J., Yang, K. R.,
24 Merchant, S. S., Truhlar, D. G., and Green, W. H., *J. Am. Chem. Soc.*, **2013**, *135*,
25 11100-11114.
26
27

1 Table 1. Nomination of some representative species in *n*-heptane sub mechanism.

nC_7H_{16}	
\dot{C}_7H_{15-1}	
C_7H_{14-1}	
$C_7H_{15}O_2-2$	
$\dot{C}_7H_{14}OOH_2-4$	
$C_7H_{14}O_2-5$	
$C_7H_{14}OOH_2-4O_2$	
$\dot{C}_7H_{13}Q_{13-5}$	
$C_7KET1-3$	
$C_7KET1-3O$	

2

3

1 Table 2. Modifications to the reaction rate rules.

Reaction	Rate rules	Details	Example
$\dot{R}O_2 \rightleftharpoons \dot{Q}OOH$	Table 6 in [68]	A × 0.5 for those using nearest analogy, which were not calculated:	
		5 member ring, O ₂ on secondary, abstraction on primary	$\dot{C}_7H_{15}O_2-2 \rightleftharpoons \dot{C}_7H_{14}OOH2-1$
		7 member ring, O ₂ on secondary, abstraction on secondary	$\dot{C}_7H_{15}O_2-2 \rightleftharpoons \dot{C}_7H_{14}OOH2-5$
		8 member ring, O ₂ on secondary, abstraction on primary	$\dot{C}_7H_{15}O_2-2 \rightleftharpoons \dot{C}_7H_{14}OOH2-6$
Cyclic ether formation	Table 3 in [72]	All A factors × 0.5	
		Ea+1 kcal for:	
		CY/C4O, OOH on primary, radical on secondary	$\dot{C}_7H_{14}OOH1-4 \rightleftharpoons C_7H_{14}O1-4+\dot{O}H$
		CY/C3O, OOH on secondary, radical on secondary	$\dot{C}_7H_{14}OOH2-4 \rightleftharpoons C_7H_{14}O2-4+\dot{O}H$
		Ea-1 kcal for:	
		CY/C4O, OOH on secondary, radical on secondary	$\dot{C}_7H_{14}OOH2-5 \rightleftharpoons C_7H_{14}O2-5+\dot{O}H$
Concerted $\dot{H}O_2$ elimination	Table 4 of [71]	A × 1.5 for:	
		O ₂ on primary, H on secondary	$\dot{C}_7H_{15}O_2-1 \rightleftharpoons C_7H_{14}-1 + \dot{H}O_2$
		O ₂ on secondary, H on primary	$\dot{C}_7H_{15}O_2-2 \rightleftharpoons C_7H_{14}-1 + \dot{H}O_2$
		O ₂ on S11, H on S11. (P1-S10-S11-S11-S10-P1)	$\dot{C}_7H_{15}O_2-3 \rightleftharpoons C_7H_{14}-3 + \dot{H}O_2$
Second addition to O ₂	Table IV of [69]	A × 0.5 from the first addition to O ₂	$\dot{C}_7H_{14}OOH1-2+O_2 \rightleftharpoons C_7H_{14}OOH1-2\dot{O}_2$

2

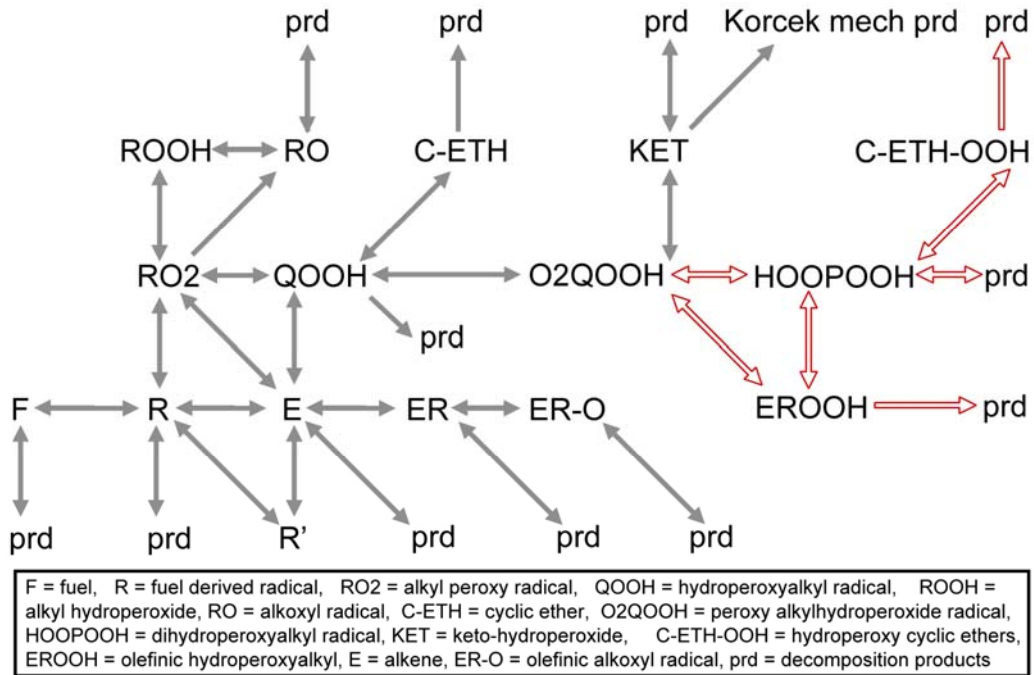
3

1 Table 3. The detailed composition of the reactant mixtures in jet-stirred reactor experiments.

φ	Inlet concentration (%)		
	<i>n</i> -heptane	O ₂	He
4.00	0.50	1.38	98.13
2.00	0.50	2.75	96.75
0.25	0.50	22.00	77.50

2

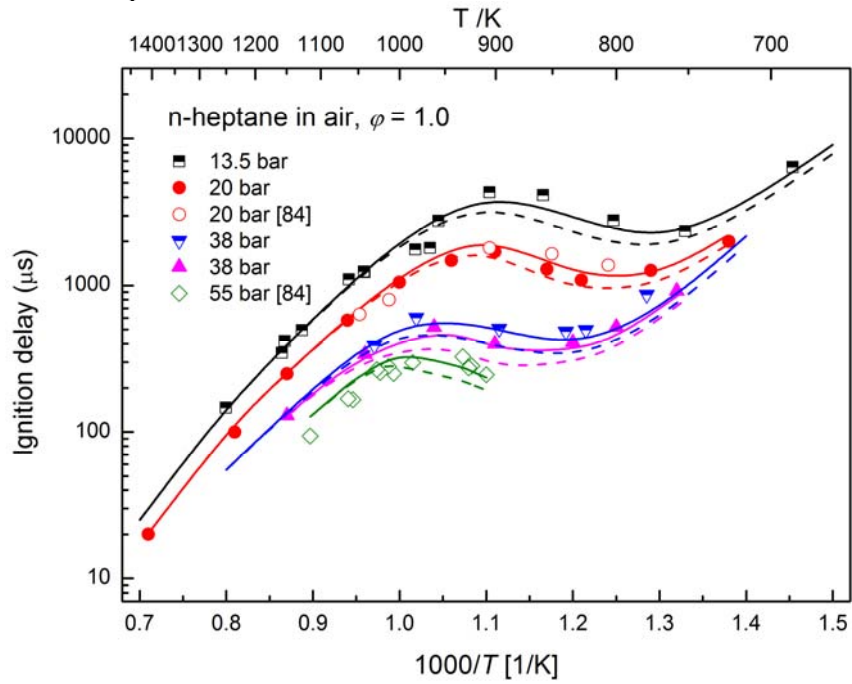
1 Figure 1. Reaction pathways considered in the model development of this work. The reaction pathways
 2 induced by the alternative isomerization of peroxy hydroperoxyalkyl have been marked with open
 3 arrows.



4

5

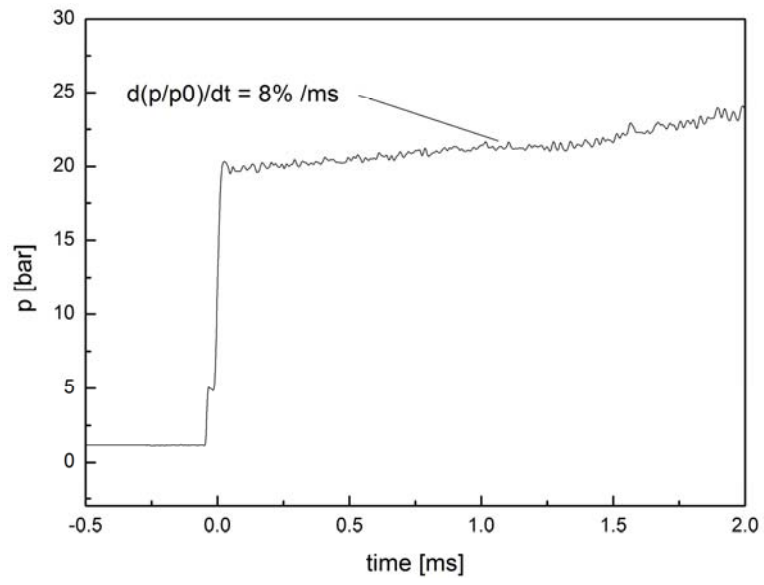
1 Figure 2. Experimental (symbols) and modeling results (lines) for *n*-heptane ignition delay times at
 2 multiple conditions (in air, $\phi = 1.0$). Half-filled symbols are experimental data from [82], while solid
 3 symbols are experimental data measured in this work. Open symbols are experimental data from [83].
 4 Solid and dashed lines are predictions with and without the modifications in the rate rules, respectively.



5

6

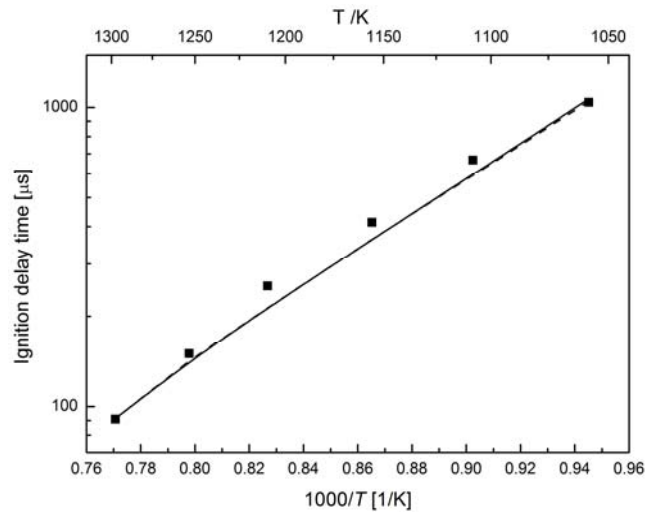
1 Figure 3. An example non-reactive pressure trace
2



3

4

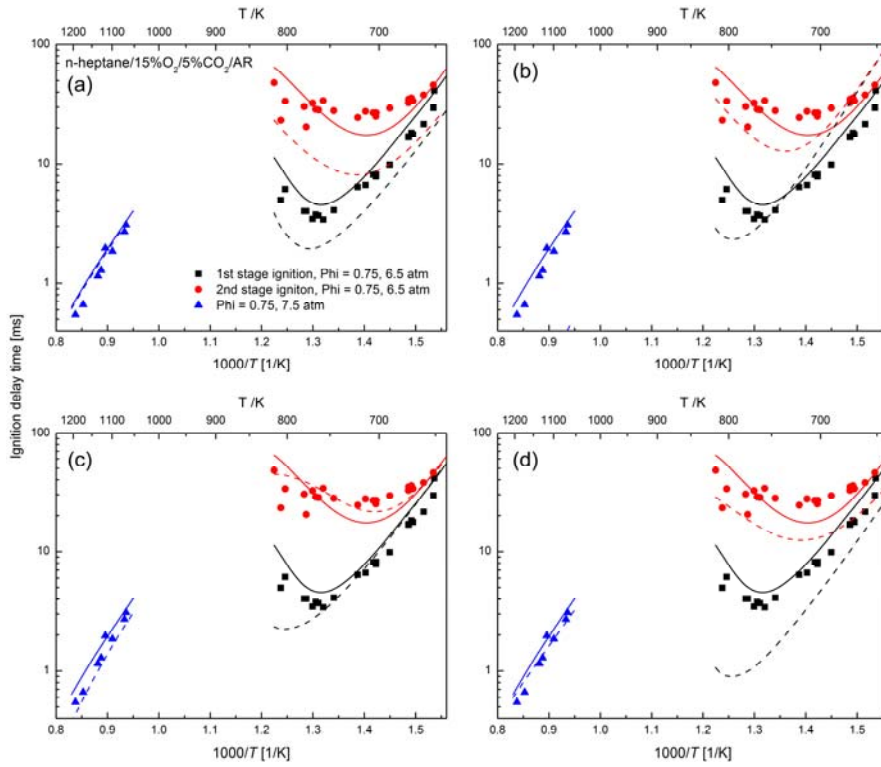
- 1 Figure 4. Experimental (symbols) and modeling results (lines) for ignition delay times of stoichiometric
- 2 *n*-heptane/air mixture at 15 bar. Solid and dashed lines are predictions with and without the
- 3 modifications in the rate rules, respectively.



4

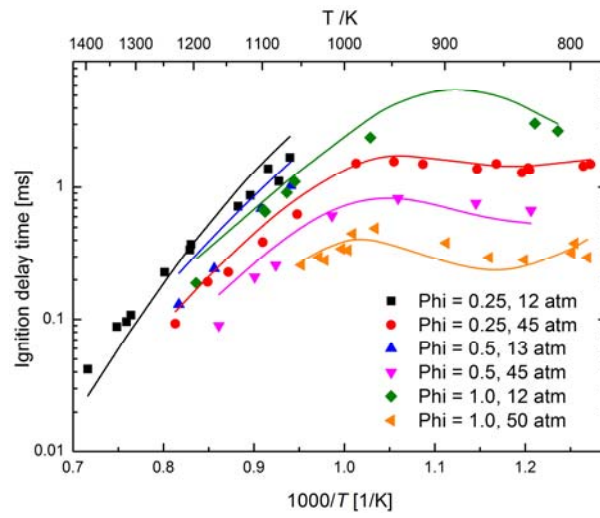
5

1 Figure 5. Experimental (symbols) [86] and modeling results (lines) for *n*-heptane/15%O₂/5%CO₂/Ar
2 mixture ignition delay times at multiple conditions. Solid lines are predictions using current mechanism
3 and dashed lines are predictions using mechanisms from (a) [42], (b) [16], (c) [30], (d) [46].
4



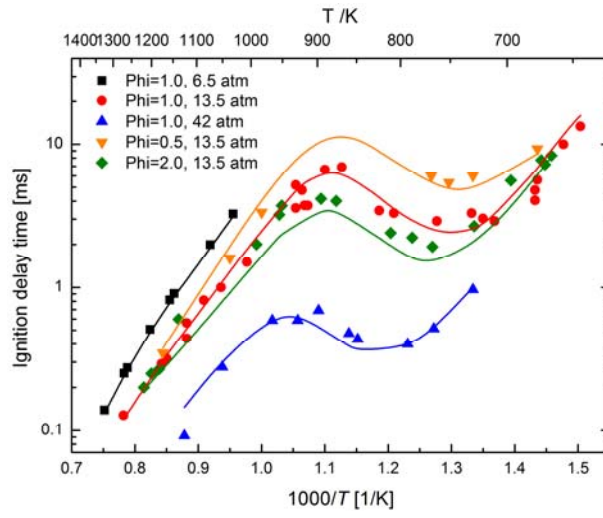
5
6

- 1 Figure 6. Experimental (symbols) [45] and modeling results (lines) for *n*-heptane/air mixture ignition
- 2 delay times at multiple conditions.
- 3



- 4
- 5

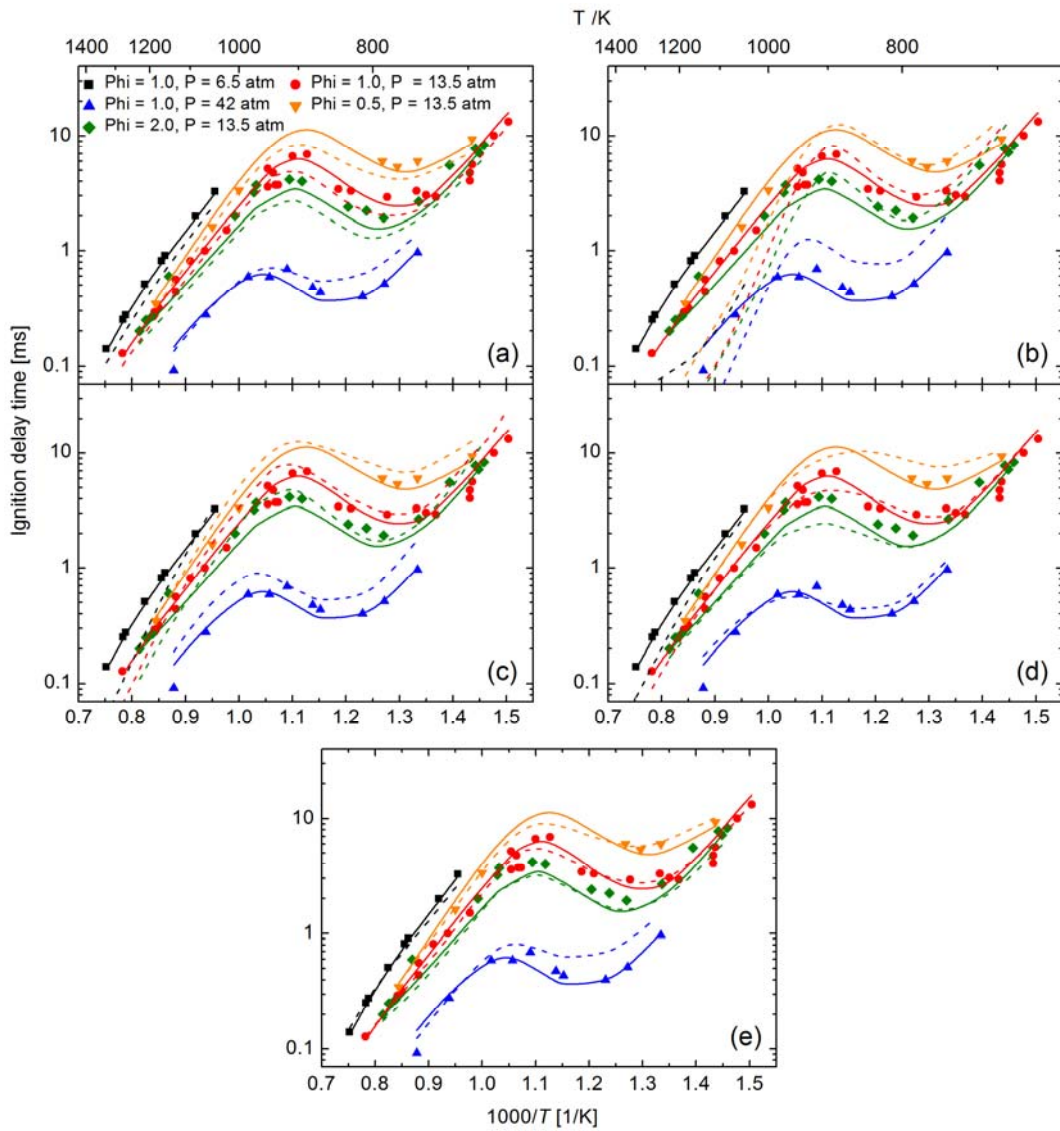
- 1 Figure 7. Experimental (symbols) [5] and modeling results (lines) for *n*-heptane/air mixture ignition delay times at multiple conditions.
- 2



3

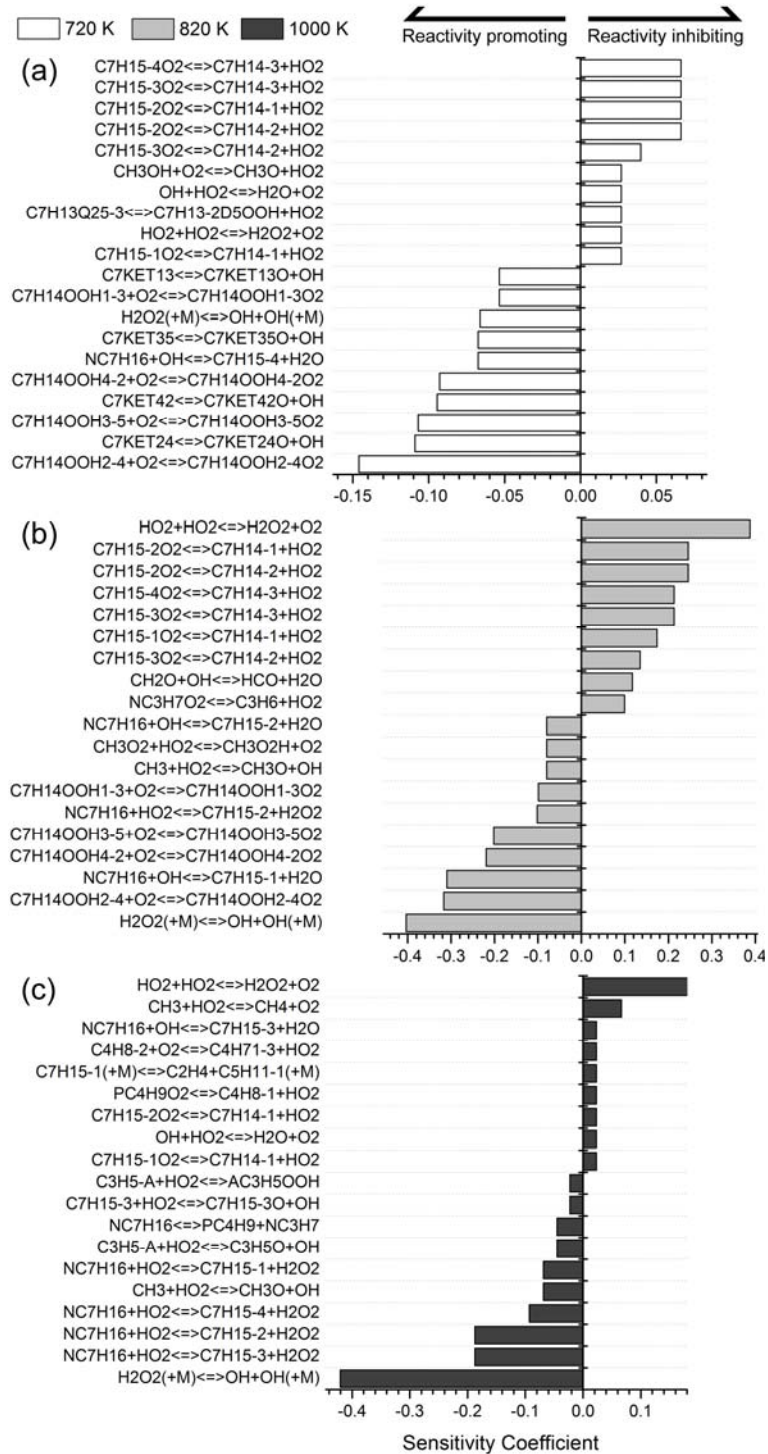
4

1 Figure 8. Comparisons of the predicted ignition delay times at multiple conditions using the current
 2 mechanism and several other ones proposed recently. Experimental data (symbols) are from [5]. Solid
 3 lines are predictions using current mechanism. Dashed lines are predictions using mechanisms from: (a)
 4 [42], (b) [16], (c) [44], (d) [30], (e) [46].



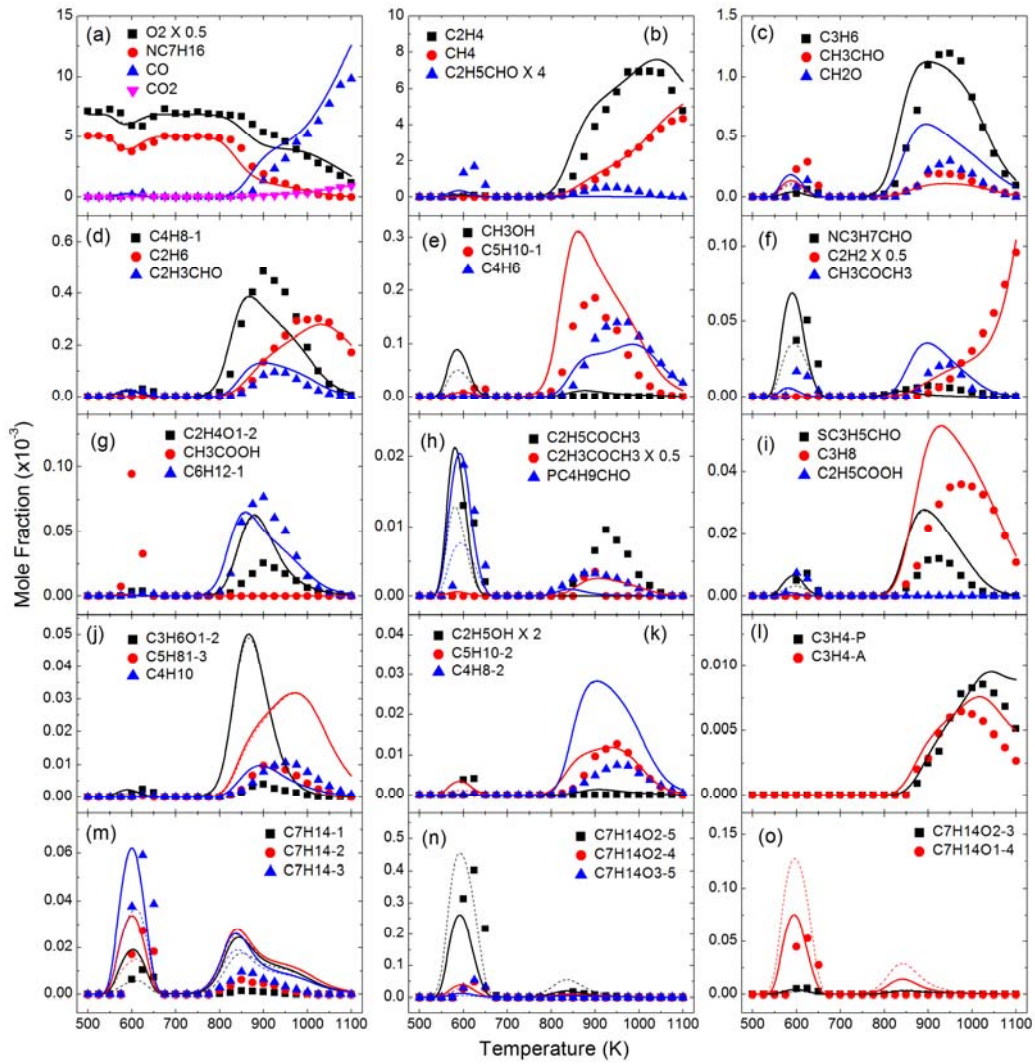
5
 6
 7

1 Figure 9. Sensitivity analysis on the ignition delay time of *n*-heptane at $T = 720$ K, 820 K and 1000 K, p
 2 = 20 bar. Negative sensitivity coefficients indicate decreases in ignition delay times.



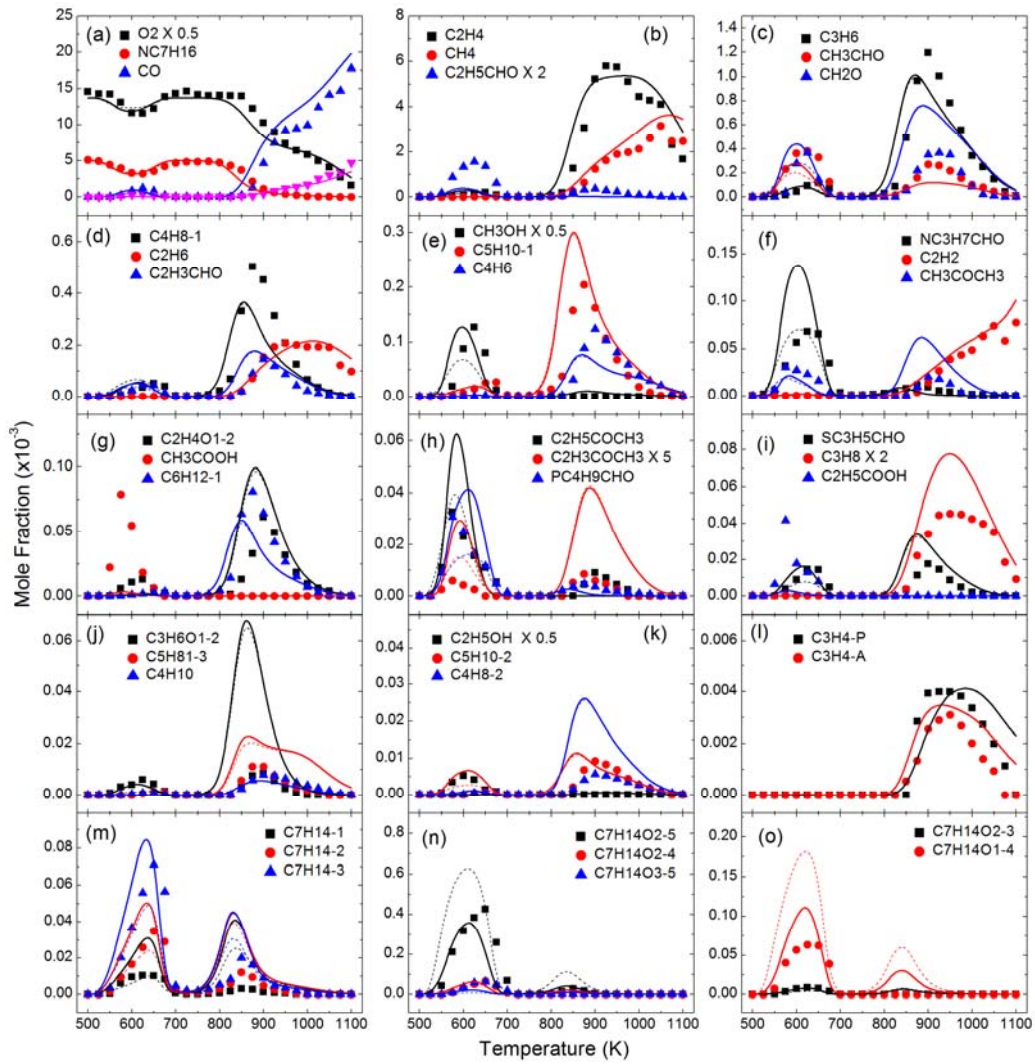
3
 4
 5
 6

1 Figure 10. Experimental (symbols) and modeling results (lines) for *n*-heptane oxidation in jet-stirred
 2 reactor at 1.06 bar with residence time = 2 s, $\phi = 4.0$, 0.5% fuel diluted by helium. Solid and dashed
 3 lines are predictions with and without the modifications in the rate rules, respectively.



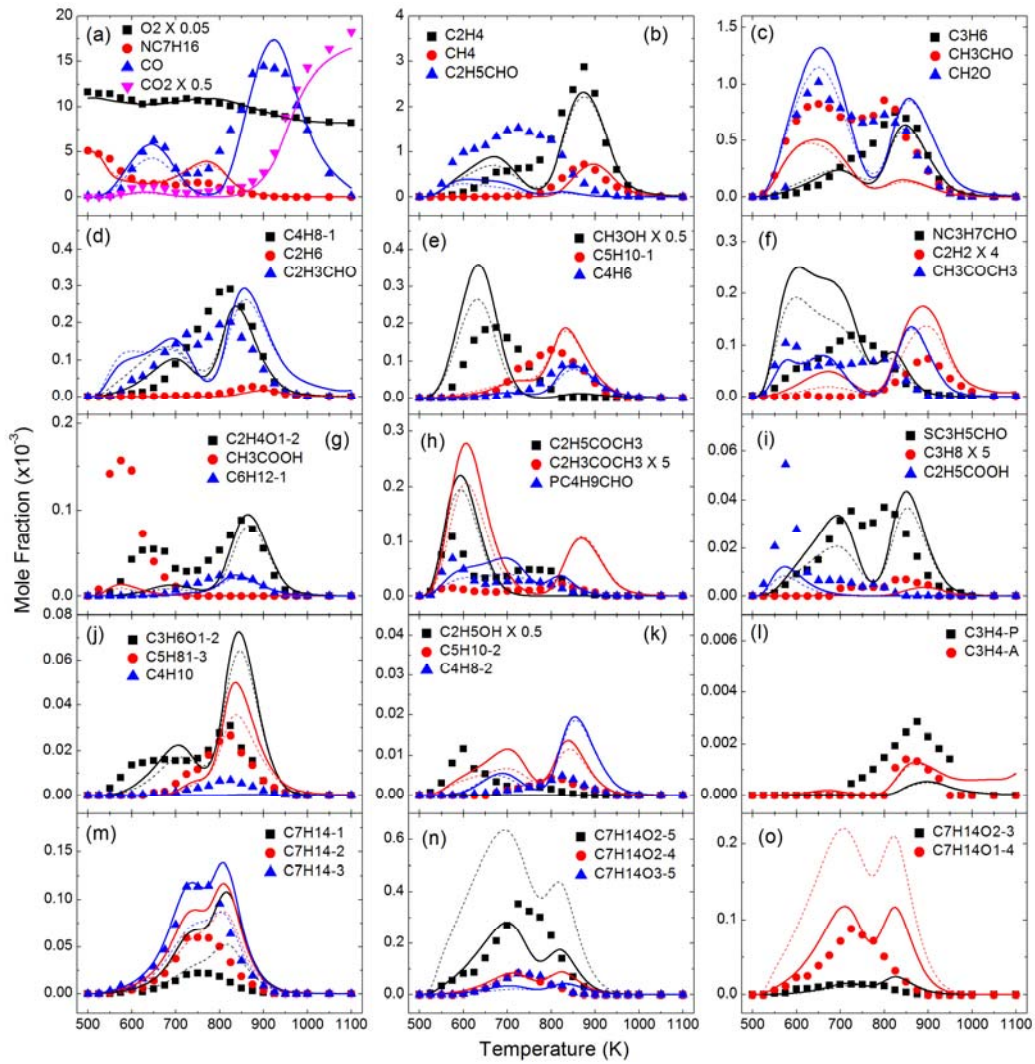
4
5
6

1 Figure 11. Experimental (symbols) and modeling results (lines) for *n*-heptane oxidation in jet-stirred
 2 reactor at 1.06 bar with residence time = 2 s, $\phi = 2.0$, 0.5% fuel diluted by helium. Solid and dashed
 3 lines are predictions with and without the modifications in the rate rules, respectively.



4
5
6

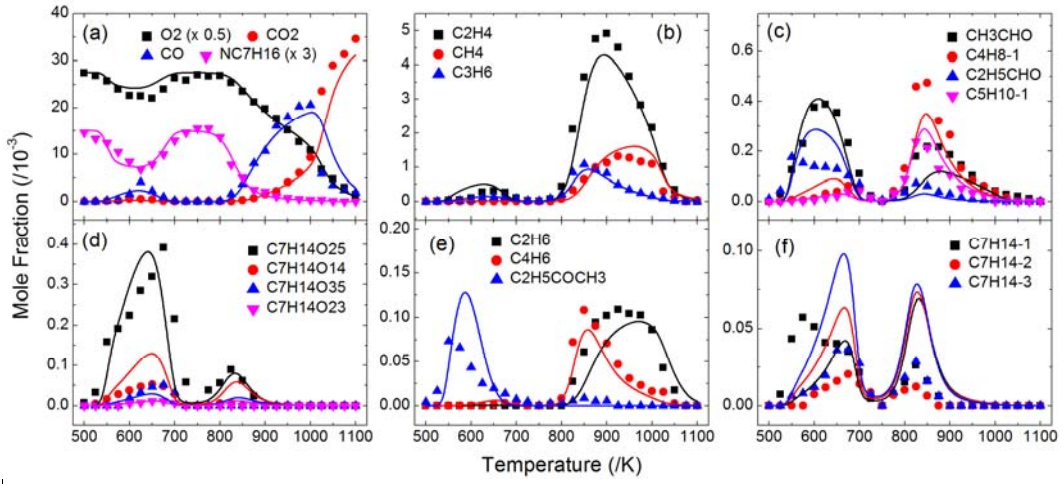
1 Figure 12. Experimental (symbols) and modeling results (lines) for *n*-heptane oxidation in jet-stirred
 2 reactor at 1.06 bar with residence time = 2 s, $\phi = 0.25$, 0.5% fuel diluted by helium. Solid and dashed
 3 lines are predictions with and without the modifications in the rate rules, respectively.



4

5

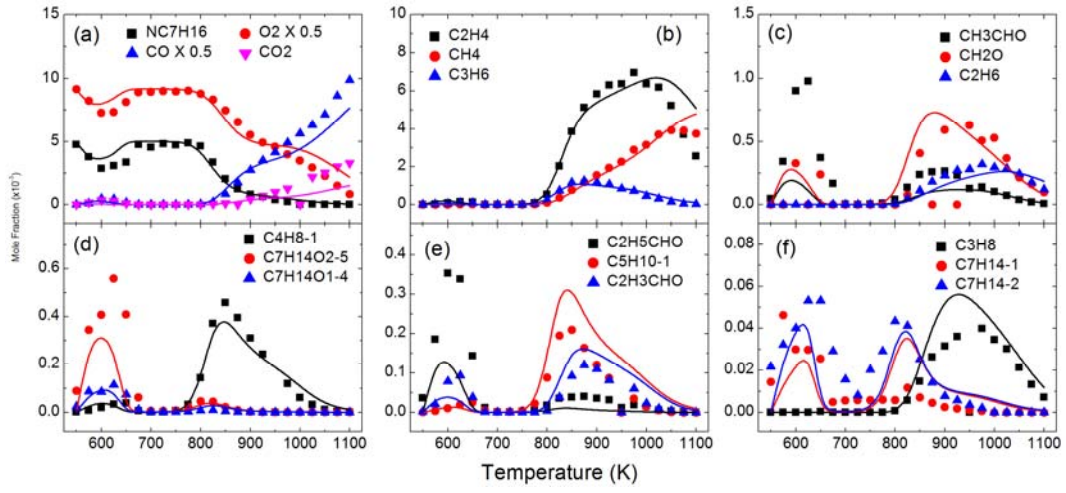
1 Figure 13. Experimental (symbols) [16] and modeling results (lines) for *n*-heptane oxidation in jet-
 2 stirred reactor at 1.06 bar with residence time = 2 s, $\phi = 1.0$, 0.5% fuel diluted by helium.



3

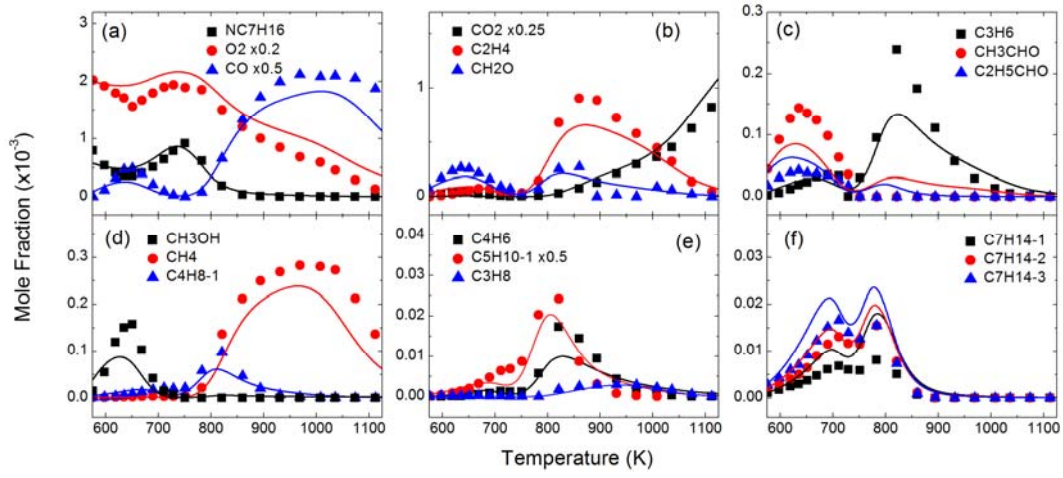
4

1 Figure 14. Experimental (symbols) [17] and modeling results (lines) for *n*-heptane oxidation in jet-
 2 stirred reactor at 1.06 bar with residence time = 2 s, $\phi = 3.0$, 0.5% fuel diluted by helium.
 3



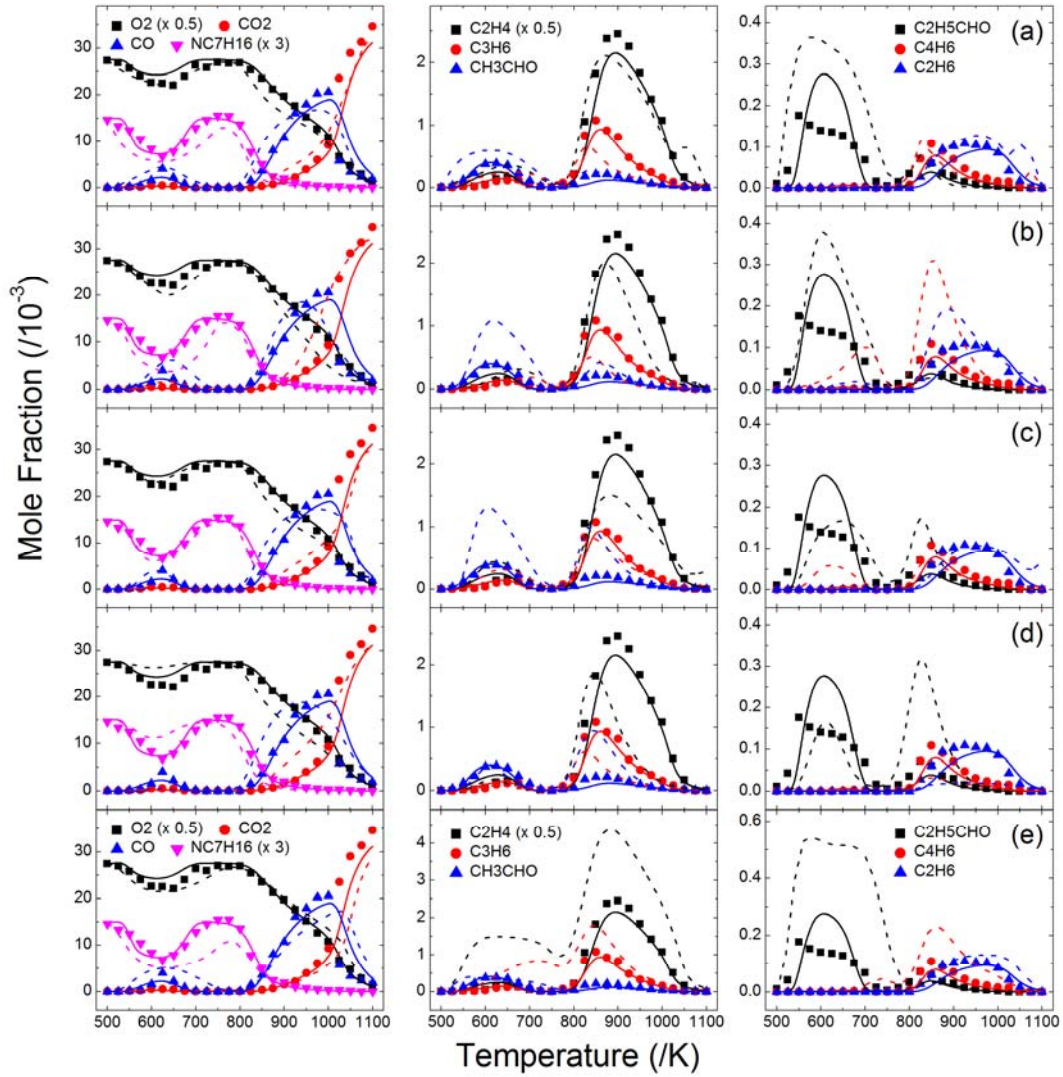
4
5

1 Figure 15. Experimental (symbols)[17] [14] and modeling results (lines) for *n*-heptane oxidation in jet-
2 stirred reactor at 10 bar with residence time = 1 s, $\phi = 1.0$, 0.1% fuel diluted by nitrogen.
3



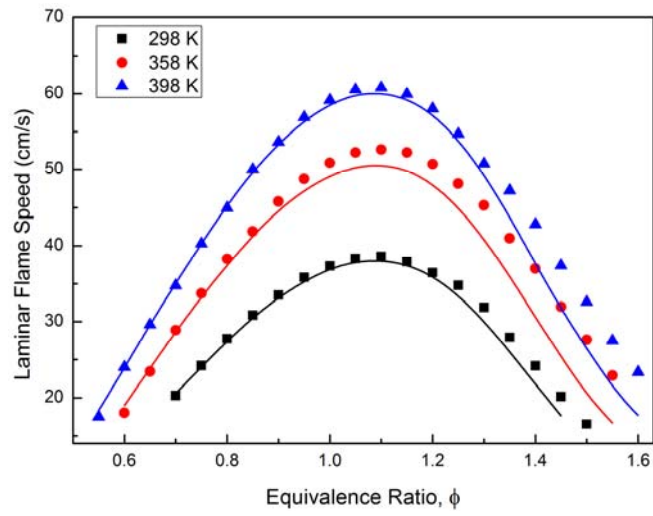
4
5

1 Figure 16. Comparisons of experimental results (symbols) [16] and predictions using the current
 2 mechanism and several other ones proposed recently. Solid lines are predictions using current
 3 mechanism. Dashed lines are predictions using mechanisms from: Row (a) [42], Row (b) [16], Row (c)
 4 [44], Row (d) [30], Row (e) [46].
 5



6
7

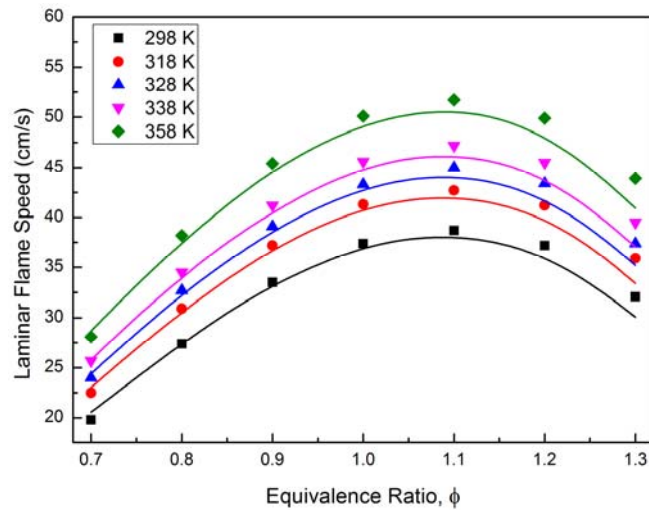
- 1 Figure 18. Experimental (symbols) [26] and modeling results (lines) for the laminar flame speed of *n*-
- 2 heptane in air at 1 atm and different initial temperatures.



3

4

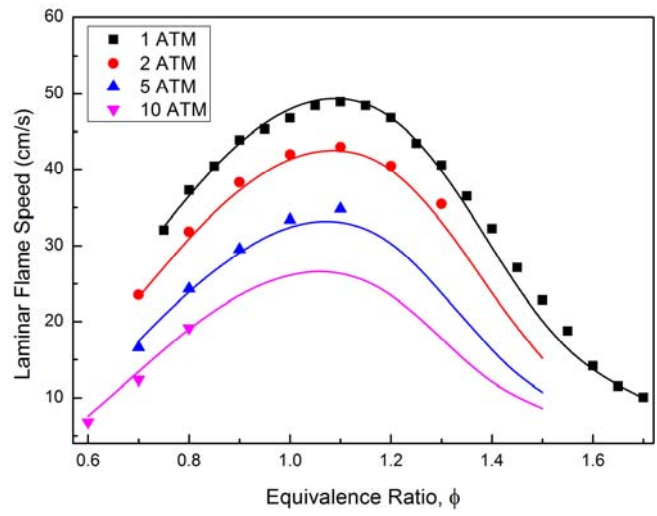
1 Figure 19. Experimental (symbols) [25] and modeling results (lines) for the laminar flame speed of *n*-
2 heptane in air at 1 atm and different initial temperatures.
3



4

5

- 1 Figure 20. Experimental (symbols) [24] and modeling results (lines) for the laminar flame speed of *n*-heptane in air at initial temperature of 353 K and different pressures.
- 2



3

4